Prediction of unsteady slug flow in a long curved inclined riser with a slug tracking model.

PADRINO, J.C., SRINIL, N., KURUSHINA, V. and SWAILES, D.

2023

International Journal of Multiphase Flow 162 (2023) 104410

Contents lists available at ScienceDirect

International Journal of Multiphase Flow

journal homepage: www.elsevier.com/locate/ijmulflow

Prediction of unsteady slug flow in a long curved inclined riser with a slug tracking model

Juan C. Padrino [a,*], Narakorn Srinil [a], Victoria Kurushina [a], David Swailes [b]

[a] School of Engineering, Newcastle University, United Kingdom
[b] School of Mathematics, Statistics and Physics, Newcastle University, Newcastle upon Tyne, NE1 7RU, United Kingdom

ARTICLE INFO

Keywords:
Slug flow
Mechanistic model
Slug tracking
Multiphase flow
Catenary riser

ABSTRACT

An improved one-dimensional mechanistic model is presented for the prediction of unsteady gas–liquid slug flows in inclined curved pipes, using the slug tracking approach. The equations for mass and momentum conservation are applied to the slug body, liquid film, and elongated bubble regions constituting a slug unit cell. The proposed model can be applied to horizontal or inclined upward flows. Statements of mass conservation result in axial changes of the liquid and gas velocities in the liquid film and elongated bubble. The slug initiation at the inlet is modelled as a random process with slug length variations. Closure relationships for the bubble nose velocity, modified by the wake effect, and the slug frequency for slug initiation are employed. The discretized governing equations are solved fully implicitly, introducing numerical treatments associated with the outlet boundary conditions and the merging of slug units. Of practical interest is an upward gas–liquid slug flow in a catenary riser with a high aspect ratio (length over diameter) being an order of a thousand representing an offshore subsea pipe for the oil and gas production. By considering the pipe initially fully filled with the travelling liquid, the dynamic scenario of the pipe transporting successive slug units is simulated, capturing the continuing evolution of slug flow patterns along the pipe exhibiting the disappearances of liquid slugs due to the bubble coalescences. Spatio-temporal variations of the liquid holdup, the pressure and its gradient, the film and slug lengths, the slug frequency, the velocities of the slug front, bubble nose, liquid in the slug body and film, and of the gas in the elongated bubble are evaluated. The backward flow occurrence in the film zone near the outlet is also predicted due to the pipe inclination. Parametric investigations are performed by specifying the superficial liquid and gas velocities, and comparing the cases of catenary pipes (with variable inclinations) versus inclined and horizontal straight pipes (with fixed inclinations). Results highlight the important effect of gas-to-oil superficial velocity ratio (GOR) in combination with the pipe inclination and curvature effects. Fluctuations of slug flow properties appear to be considerably amplified and more intermittent when increasing the GOR. This observation is important towards regulating the practical flow rates for subsea oil and gas productions as well as designing flexible pipes subject to slug flow-induced vibrations.

1. Introduction

One-dimensional (1D) mechanistic models and associated numerical treatments have been improved over the years and applied to predict the multiphase characteristics of internal flows in long rigid pipes, displaying low input complexity and affordable computational time (Taitel and Barnea, 1990b; Gomez et al., 2000; Petalas and Aziz, 2000; Zhang et al., 2003a; Shoham, 2006). Of theoretical and practical interest is the gas–liquid intermittent slug flow comprising a train of alternating liquid slugs and elongated gas bubbles accompanied by variable-thickness liquid films. An unaccounted occurrence or inaccurate prediction of slug flows may result in a sudden operational disruption, failure and related expensive cost. Ongoing research effort to advance a mechanistic model is carried out by transforming the complex three-dimensional (3D) multiphase fluid dynamics to the 1D balance equations supported by several closure relationships and expressions of a heuristic nature. This approach is found to be increasingly helpful when the multi-fluid characteristics are estimated for a high aspect ratio pipe with a length-to-diameter ratio being an order of a hundred or thousand, that would, otherwise, involve significant computational costs with the Computational Fluid Dynamics (CFD) approach (Hirt and Nichols,

* Corresponding author.
E-mail addresses: juan.padrino@newcastle.ac.uk, padr0006@umn.edu (J.C. Padrino).

https://doi.org/10.1016/j.ijmultiphaseflow.2023.104410
Received 9 June 2022; Received in revised form 4 November 2022; Accepted 3 February 2023
Available online 8 February 2023

Nomenclature

A	Pipe internal cross-sectional area
A_0, B_0, C_0, K_0	Coefficients in catenary equations
C_1, C_2, C_3	Coefficients for wake effect factor
C_s	Coefficient for bubble nose velocity
C_τ	Coefficient in friction factor formula
d	Pipe internal or hydraulic diameter
f	Friction factor
Fr	Froude number
g	Gravitational acceleration
GOR	Gas-to-oil superficial velocity ratio
h_f	Film thickness
j	Superficial velocity
l	Film, slug body, or unit cell length
L	Pipe length
N	Number of slug unit or liquid-only cells
P	Pressure
$\mathcal{R}$	Film length to slug body length ratio
Re	Reynolds number
s	Arc-length coordinate
S	Pipe internal perimeter
t	Time
u	Local phase velocity
$\overline{u}$	Length-averaged phase velocity
u_0	Drift velocity of the elongated bubble
u_t	Bubble nose translational velocity
$u_{t\infty}$	Bubble nose translational velocity without wake effect
x, y	Cartesian coordinates
z	Axial coordinate within the elongated bubble-film or slug body regions
α	Liquid holdup or void fraction
ζ	Spatial coordinate at a cross section
η	Elongated bubble nose position
θ	Pipe local inclination angle with respect to the horizontal
Θ	Factor in slug frequency correlation
λ	Angle subtended by the gas–liquid interface
λ_l	Non-slip liquid holdup
μ	Fluid dynamic viscosity
μ_N	Mean of logarithmic values
ξ	Slug body front position
$\dot{\xi}$	Slug body front velocity
ρ	Fluid density
σ_L	Standard deviation of log-normal distribution for slug body length
σ_N	Standard deviation of logarithmic values
Σ	Centroid of film or elongated-bubble cross section
τ	Shear stress
Φ, Ψ	Factor in slug frequency correlation
ω_P	Pressure frequency
ω_s	Slug frequency

Subscripts

e	Elongated bubble-film region tail
f	Liquid film
g	Gas
in	Pipe inlet
l	Liquid
o	Elongated bubble nose
s	Slug body
$s\xi$	Inside slug body, at position ξ
$s\eta$	Inside slug body, at position η
u	Unit cell

Superscripts

a	Quantity of cell after merging
j	Unit cell index
m	Exponent in friction factor formula
n	Time level
$*$	Quantity of the exiting unit cell at a specific instant

1981; Sivier et al., 1993; Ferziger and Perić, 2002; Prosperetti and Tryggvason, 2009; Zikanov, 2019). Therefore, mechanistic models provide a cost-efficient solution to CFD problems related to the multiple phase transportations in several industries including the petroleum oil and gas production, chemical and manufacturing process, nuclear and geothermal energy. Several numerical industrial tools have been developed such as OLGA (Bendiksen et al., 1991), Petra (Larsen et al., 1997), TUFFP (Zhang et al., 2003a,b), LedaFlow (Issa and Kempf, 2003; Danielson et al., 2005), TACITE (Irfansyah et al., 2005), SLUGGIT (Kjeldby et al., 2011; Kjeldby and Nydal, 2012; Ortega et al., 2012, 2013) and 5ESCARGOTS (Ferrari et al., 2019). Nevertheless, forecasting the spatio-temporal properties of unstable gas–liquid slug flows in a long inclined curved pipe/riser using 1D models remains a challenging task, owing to the complex flow pattern evolutions and multiphase interaction phenomena caused by different fluid properties and the structural geometry with variable inclination and curvature along the curved pipe. These are manifested by the unsteadiness of fluid pressure, momentum and void fraction fluctuations as well as transient features of flow regimes. The present study aims to address these challenges through advancing a 1D model and implementing the numerical methodologies based on the slug tracking approach for arbitrarily inclined curved risers.

Classification of 1D mechanistic models for the regime of alternating gas and liquid plugs is well documented in the literature (Shoham, 2006; Mazza et al., 2010; Nydal, 2012; Rosa et al., 2015). The general idea behind the flow simplification is considering the flow as a train of axially propagating ‘slug units’ or ‘unit cells’, each of them comprising one region filled predominantly with liquid, called ‘liquid slug’ or ‘slug body’, and one region with an elongated bubble accompanied by a liquid film over the surface of the pipe annulus. In the order of an increasing precision and computational time, models of a steady-state, slug tracking, hybrid and slug capturing type could be identified as four main methods operating within a Lagrangian or Eulerian framework. The hybrid model combines the slug tracking and capturing approaches. In this case, the slug capturing part of the approach dictates a refined discretization of the film region of a slug unit, which is treated with the two-fluid model, as this region shows a stratified configuration. On the other hand, the liquid slug bodies are treated as in the slug tracking method. See below for appropriate references on the hybrid model. In general, a 1D mechanistic model requires the inputs of phase fundamental properties (e.g., densities, viscosities, surface tension) and geometric dimensions of the conveying pipe (diameter, length, inclination) (Taitel and Dukler, 1976; Taitel and Barnea, 1990b; Barnea, 1990; Zhang et al., 2000; Chatjigeorgiou, 2017; Ma and Srinil, 2020). Closure relationships are further involved

in obtaining the supporting quantities including, e.g., the translational flow velocity (Nicklin, 1962; Bendiksen, 1984; Théron, 1989; Petalas and Aziz, 2000), slug length (Brill et al., 1981; Gordon and Fairhurst, 1987), slug liquid holdup (Gregory et al., 1978; Barnea and Brauner, 1985; Andreussi and Bendiksen, 1989), wetted wall fraction (Meng, 1999) and interfacial friction factor (Grolman and Fortuin, 1997). The majority of these empirical expressions have been derived based on the statistical analysis of experimental data at specific flow-structure conditions. The influence of closure relations has been reviewed and investigated in several studies (Al-Safran, 2009; Brustur, 2014; Roullier et al., 2017; Mohammadi et al., 2019; Zanganeh et al., 2020). With closure correlations, mass and momentum balance equations are then solved in order to obtain quantities characterizing the unit cells (film lengths, liquid holdups, liquid–gas velocities, pressure variations). Hence, 3D properties of actual internal flows are estimated through filtering of statistical correlations to 1D flow characteristics.

A further distinction in the simulation workflow of mechanistic models is related to the numerical treatment. For steady-state flow models, such as those by Kordyban (1961), Dukler and Hubbard (1975), and Taitel and Barnea (1990a,b), time-invariant flow properties are described for each slug unit. These models only allow observing spatial variations of flow features. For unsteady flows, a slug tracking method in the Lagrangian framework may be considered (Nydal and Banerjee, 1996; Taitel and Barnea, 1998; Al-Safran et al., 2004; Ujang et al., 2006; Xin et al., 2006; Rosa et al., 2015; Grigoleto et al., 2021). These models compute the position and velocity of the elongated bubble front and tail, that also indicates the start and end of the film zone. Mass, momentum and energy balances are solved for a single control volume of the liquid slug, for the large bubble and the liquid film. Slug tracking models display a wide range of complexity, and calculations of the film zone may be simplified by omitting the momentum balance for the gas bubble. The model complexity may also arise due to the incorporated slug initiation and dissipation mechanisms or the consideration of non-uniform thickness of the liquid film along the axial coordinate. A physical reason for this film non-uniformity may be due to the propagation of waves and the eddy formation in the liquid slug (Dukler and Hubbard, 1975). Relevant flow pattern maps (Mandhane et al., 1974; Spedding, 1980; Barnea et al., 1980; Mukherjee and Brill, 1985; Wu et al., 2017; Fan et al., 2019), may be used for characterizing the two-phase flow regime and associated parametric ranges. One of the recent challenges for the slug tracking approach is the consideration of a high aspect ratio pipe and associated numerical strategies for yielding the solution convergence (Ortega et al., 2018; Vásquez and Avila, 2021). This challenge will be accounted for in the present work considering a very long inclined curved pipe, based on the slug tracking approach.

Among the earliest efforts on slug tracking, the works of Barnea and Taitel (1993), Zheng et al. (1994), Taitel and Barnea (1998), and Xin et al. (2006) may be referred to. More sophisticated applications of the slug tracking may be found in Nydal and Banerjee (1996), Al-Safran et al. (2004), Ujang et al. (2006), Rosa et al. (2015), and Grigoleto et al. (2021), the latter also including the temperature variation. With the exception of the model in Nydal and Banerjee (1996), the so-called quasi-equilibrium or quasi-steady approximation, which neglects some of the unsteady terms in the equations of mass and momentum conservation as well as the momentum fluxes, has been adopted in these models. For Al-Safran et al. (2004) and Ujang et al. (2006), the steady momentum equations of Taitel and Barnea (1990b,a) have been applied to the slug body, elongated bubble, and liquid film of uniform thickness. For Rosa et al. (2015) and Grigoleto et al. (2021), the rate of change of momentum in the slug body is included; yet, analogous rates of change remain absent in the descriptions of the elongated bubble and liquid film. Momentum fluxes are considered in their studies. Further, Grigoleto et al. (2021) included a pressure difference, given in terms of a momentum flux, to account for the head loss generated by the liquid recirculation in the wake of the elongated bubble. Recently, a slug tracking model has been presented by Vásquez and Avila (2021) for a problem of slug flow-induced vibration in a flexible curved riser. With respect to the hydrodynamic slug model, their work applies the momentum equation for the slug body, containing no gas, considering the rate of change of momentum and the momentum fluxes at the boundaries of the control volume. The model has the merit that a single slug body can span several pipe sections of different inclinations at a given time. It also considers coalescence of consecutive unit cells. However, the model does not consider the momentum equations for the liquid film and elongated bubble during the tracking of the slug units, assuming that the film holdup does not vary in time, and neglecting the random effects commonly considered in the slug tracking models. It is unclear how the velocities of the liquid in the film and the gas in the elongated bubble are updated as a slug unit moves along the inclined curved pipe. These features will be herein discussed in detail.

In the present study, we will focus on the development of a slug tracking model due to its capability to describe the slug flow unsteadiness and convey the analysis in a time-efficient manner, compared to the slug capturing (Issa and Kempf, 2003; Renault, 2007; Bonizzi et al., 2009), hybrid tracking–capturing (Kjølaas, 2007; Kjeldby et al., 2011; Nydal, 2012) or even CFD (Batchvarov et al., 2020; Shin et al., 2018; Constante-Amores et al., 2021; Valdés et al., 2022; Heaney et al., 2022) methodologies. The representative model of the slug tracking proposed by Nydal and Banerjee (1996) serves as a predecessor to the mathematical formulation in the present study. Nydal and Banerjee (1996) considered the mass balances for the slug body (with no gas), the elongated bubble, and the liquid film in an unsteady form. For the liquid film, they assumed a uniform thickness, and unsteady momentum balances were applied to the liquid slug zone and the liquid film, while the pressure was considered uniform across the gas bubble, so that the model does not require a momentum balance for the gas bubble. Unlike the present effort, their approach does not describe changes in the liquid film velocity with the variation of the axial coordinate. The recently postulated model in Padrino et al. (2021), applied to straight inclined pipes, represents a departure from the model in Nydal and Banerjee (1996). The starting point is given by the equations of mass and momentum conservation written in integral form for the various structures of a slug flow unit, namely, the slug body, the liquid film (assumed to be spatially uniform), and the elongated bubble. Unsteady terms are kept in the equations describing the slug body and stratified region, and the pressure is not considered uniform in the latter. Mass and momentum balances are also prescribed for the borders shared between the slug body and neighbouring stratified regions, yielding velocity and pressure ‘jumps’. Within the Lagrangian framework, the positions of the various structures of the flow are tracked over time. The two-phase mixture can move in the horizontal or sloping directions. Under unsteady conditions, although the film thickness does not vary in space, statements of mass conservation for the stratified region result in axially-varying fluid velocities. The solution of the resulting system of non-linear equations is obtained numerically by means of a fully implicit method.

The purpose of this study is to present a 1D mechanistic model for tracking unsteady gas–liquid slug flow in long inclined curved pipes. The model expands and improves on the previous preliminary model formulated in Padrino et al. (2021). With reference to that work, the present model has several novelties. First, a correction factor is included in the momentum exchange between the slug body and the elongated bubble-film region, taking place at the slug body tail. This accounts for a smooth contraction of the film underneath the bubble nose, in contrast with a sudden expansion at the slug body front. Second, for an upward-inclined flow, variation of the pipe’s inclination angle is allowed. Third, the slug initiation at the pipe inlet with random values for the slug body length is implemented by expanding a recent model from the literature based on the slug frequency definition. Also, merging of consecutive slug unit cells due to the wake effect is modelled using simplified mass and momentum balances. Finally, the modelling

of the flow at the outlet considers various stages, such as whether the slug body or the elongated bubble-film regions are crossing the outlet plane.

This paper is organized as follows. In Section 2, the mathematical formulation of the mass and momentum conservation laws for the slug tracking model is presented. Conditions of the flow at the pipe inlet and outlet are discussed in Section 3. The numerical treatment is described in Section 4 including the discretization of governing equations, boundary and initial conditions, and the scheme for merging of consecutive slug unit cells as well as validation of model predictions with experimental data in the literature for horizontal or upward-inclined gas–liquid flows in straight pipes. In Section 5, we apply the slug tracking model to long inclined curved risers with catenary shapes, and we parametrically investigate several unsteady slug flow characteristics by specifying the two-phase superficial velocities. The paper ends with the summary of key findings and conclusions in Section 6.

2. Model formulation for slug tracking

The present model for tracking an unsteady gas–liquid slug flow in a curved pipe is based on the following main assumptions:

- Gas and liquid flow simultaneously in a rigid pipe of circular cross section whose area, A, remains uniform throughout the entire pipe length. The internal diameter is denoted by d. The shape of the pipe is described by the Cartesian components of its axis — the curve passing through the centres of all cross sections. We assume that this axis lies in a plane, and the pipe may be curved. This position is measured by the arc-length coordinate, s, which is zero at the pipe inlet, the section where the liquid and gas enter the pipe. The pipe outlet is located at $s = L$, where L is the pipe length. The equation of the pipe axis can thus be written as $x = x(s)$ and $y = y(s)$, where x and y are the Cartesian coordinates.
- The gravity vector, which lies on the plane of the pipe, is aligned with the y axis and points in the direction of decreasing y.
- The slug flow in the pipeline is modelled as a sequence of slug unit cells. The flow field in each slug unit is one-dimensional as quantities only vary with the position along the pipe. The pressure, however, is also allowed to change linearly within a cross section at a given position to account for hydrostatic (gravity) effects. Following, for instance, Al-Safran et al. (2004) and Ujang et al. (2006), each unit cell of the gas–liquid slug flow is labelled with an (integer) index j, numbered in ascending order, with the lowest index closer to the outlet. A slug unit cell lies between positions $s = \xi^{j+1}$ and $s = \xi^{j}$, with its front (tail) at the latter (former), and it is assumed to occupy a *straight* pipe element (see Fig. 1).
- A slug unit cell comprises three regions: (i) the slug body, which in this work is assumed to contain no gas (typically in small bubbles) as in the case of Nydal and Banerjee (1996) and Rosa et al. (2015), (ii) a liquid film, and (iii) an elongated bubble. This is depicted in Fig. 1. The combined elongated bubble–liquid film region spans from ξ^{j+1} to η^{j}, and the film thickness is assumed to be uniform; the liquid slug body is bounded by positions η^{j} and ξ^{j}. Whilst positions ξ^{j} and ξ^{j+1} fall on the axis of the curved pipe, position η^{j} does not, in general, as this lies on the straight segment connecting those two points (Fig. 1). We assume the conditions are such that the flow is horizontal or inclined-upward. The slug body length, l_s^j, is given by $\xi^{j} - \eta^{j}$ and the film length, l_f^j, by $\eta^{j} - \xi^{j+1}$, both properties may change with time. The inclination angle of the straight pipe segment occupied by the slug unit cell j at a given instant with respect to the horizontal x-axis is denoted by θ^j.
- The liquid is incompressible with a constant density ρ_l whilst the gas is compressible with a density ρ_g given by the ideal gas law. The flow is isothermal. The gas density is considered to be uniform within the slug unit cell j but it may change from one unit cell to the other due to spatial pressure changes. The liquid and gas dynamic viscosities, denoted by μ_l and μ_g, respectively, are assumed constant.
- The proposed model consists of integral mass and momentum balances written for moving and deforming control volumes, as well as for the borders shared by these control volumes, which are treated as surfaces of discontinuity. These formulae are based on those presented in Panton (2013), modified here to be applied to a one-dimensional, two-phase gas–liquid flow.

The mechanistic model is based on the mass and momentum conservation statements written for the various regions of a slug unit cell. To achieve closure of the system of equations, additional expressions relating the variables appearing in those balances must be introduced. They are listed in Appendix A.

2.1. Kinematic relationships

For the slug unit cell j, at the slug front we set

$$\dot{\xi}^j = \frac{d\xi^j}{dt}, \tag{1}$$

whilst at the bubble nose, equivalent to the slug body tail, its displacement follows

$$u_t^j = \frac{d\eta^j}{dt}, \tag{2}$$

where u_t^j is the bubble nose translational velocity and t is the time. The rate of change of the slug body and the elongated bubble-film region lengths are thus given, respectively, by

$$\dot{l}_s^j = \frac{dl_s^j}{dt} = \dot{\xi}^j - u_t^j, \tag{3}$$

$$\dot{l}_f^j = \frac{dl_f^j}{dt} = u_t^j - \dot{\xi}^{j+1}. \tag{4}$$

2.2. Mass balances in a slug unit

Starting with the slug body of unit cell j, which contains no gas, we consider a control volume bounded by the pipe wall with a face at position η^j and another at an arbitrary point within the slug body, separated from the former by a distance z_s, with $0 \leqslant z_s \leqslant l_s$ (Fig. 1). This second face has thus the velocity $u_t^j + \dot{z}_s$. The equation of mass conservation for this moving control volume can be written as

$$\frac{d}{dt}\left(\rho_l z_s A\right) = \rho_l A\left(u_{ls}^j|_{\eta} - u_t^j\right) - \rho_l A\left(u_{ls}^j|_{\eta+z_s} - u_t^j - \dot{z}_s\right), \tag{5}$$

where $u_{ls}^j|_{\eta}$ and $u_{ls}^j|_{\eta+z_s}$ denote the velocities of the liquid in the slug body at positions η^j and $\eta^j + z_s$, respectively. Since ρ_l and A are constants, the balance in Eq. (5) reduces to $u_{ls}^j|_{\eta+z_s} = u_{ls}^j|_{\eta}$. Therefore, the liquid velocity u_{ls}^j does not vary spatially within the slug body of cell j and only changes with time.

Applying integral mass balances over expanding or contracting control volumes enclosing the elongated bubble and the liquid film regions results in the following one-dimensional conservation equations. For the gas in the elongated bubble, we may write

$$\frac{d}{dt}\left(\rho_g^j \alpha_g^j l_f^j A\right) = \rho_g^j \alpha_g^j\left(u_{ge}^j - \dot{\xi}^{j+}\right) - \rho_g^j \alpha_g^j\left(u_{go}^j - u_t^j\right), \tag{6}$$

where α_g^j denotes the void fraction, which does not vary axially, and u_{go}^j and u_{ge}^j are, respectively, the axial gas velocities at positions η^j and ξ^{j+1}. After making use of Eq. (4), this expression reduces to

$$\frac{d}{dt}\left(\rho_g^j \alpha_g^j\right) = \frac{\rho_g^j \alpha_g^j}{l_f^j}\left(u_{ge}^j - u_{go}^j\right). \tag{7}$$

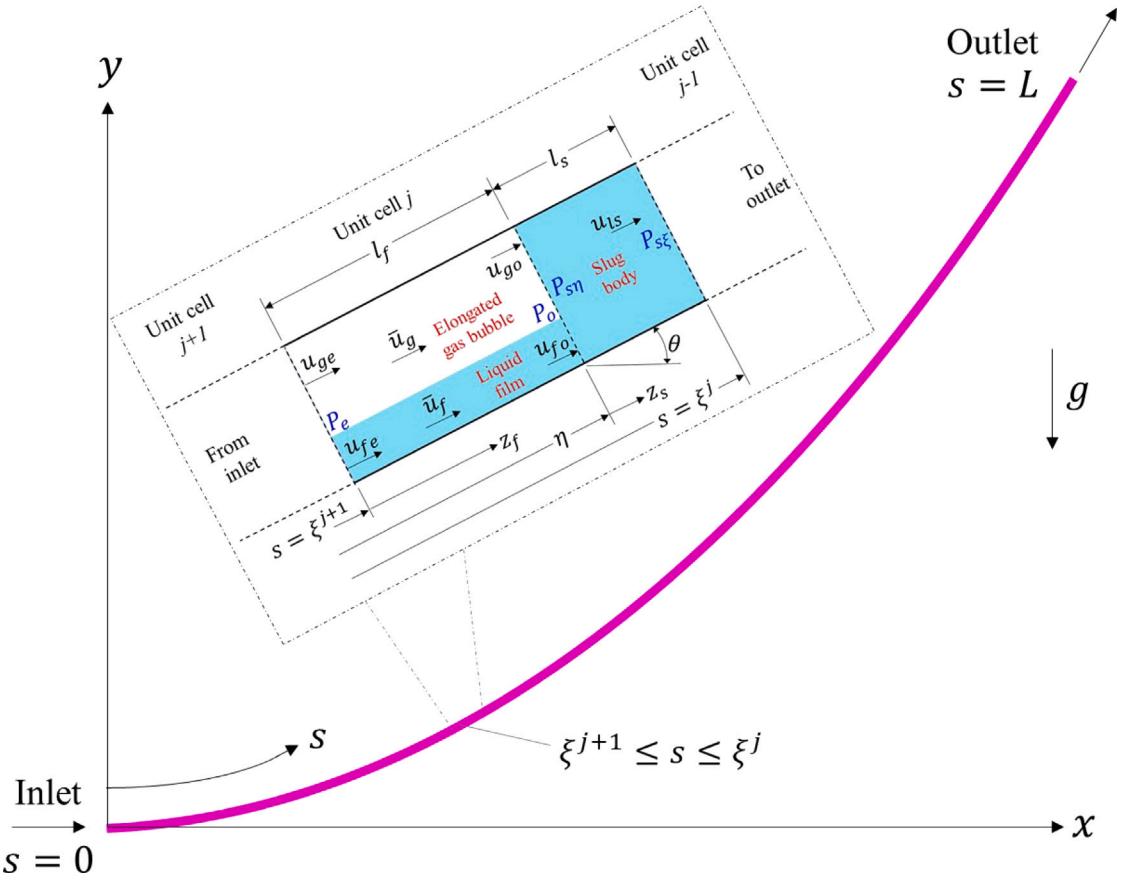

Fig. 1. Sketch of a typical slug flow unit cell in a curved pipe with upward flow. The two-phase gas–liquid slug flow in a pipeline is represented by a sequence of unit cells.

Proceeding in a similar manner with the liquid film, we have

$$\frac{d}{dt}\left(\rho_l \alpha_f^j\right) = \frac{\rho_l \alpha_f^j}{l_f^j}\left(u_{fe}^j - u_{fo}^j\right), \tag{8}$$

where α_f^j is the holdup of the liquid film, whose thickness is constant, and u_{fo}^j and u_{fe}^j denote the axial film velocities at η^j and ξ^{j+1}, respectively.

The mass conservation analysis on control volumes containing a fraction of the elongated bubble or liquid film regions described in Appendix B leads to

$$u_g^j = (1 - z_f/l_f^j)u_{ge}^j + (z_f/l_f^j)u_{go}^j, \tag{9}$$

$$u_f^j = (1 - z_f/l_f^j)u_{fe}^j + (z_f/l_f^j)u_{fo}^j, \tag{10}$$

respectively, and $0 \leqslant z_f \leqslant l_f^j$ (see Fig. 1). Integration of these expressions over the film length yields the average velocities of the gas in the elongated bubble and of the liquid film

$$\overline{u}_g^j = \left(u_{go}^j + u_{ge}^j\right)/2, \tag{11}$$

$$\overline{u}_f^j = \left(u_{fo}^j + u_{fe}^j\right)/2, \tag{12}$$

respectively. These average velocities will appear in the momentum equations, and Eqs. (11) and (12) will prove useful when closing the system of equations.

We consider the plane at position ξ^j as a surface of discontinuity. Taking into account that there is no gas in the slug body, the gas and liquid mass balances on this surface result in

$$u_{ge}^{j-1} = \dot{\xi}^j, \tag{13}$$

$$\alpha_f^{j-1}\left(u_{fe}^{j-1} - \dot{\xi}^j\right) = \left(u_{ls}^j - \dot{\xi}^j\right), \tag{14}$$

respectively. Similarly, at position η^j we have

$$u_{go}^j = u_t^j, \tag{15}$$

$$\alpha_f^j\left(u_{fo}^j - u_t^j\right) = \left(u_{ls}^j - u_t^j\right). \tag{16}$$

Finally, the liquid holdup and gas void fraction satisfy the geometric constraint

$$\alpha_f^j + \alpha_g^j = 1. \tag{17}$$

Note that when the time derivatives in Eqs. (7) and (8) are zero, the classical results for the velocities of the gas and liquid when the film has a uniform thickness, namely, $u_{go}^j = u_{ge}^j = \overline{u}_g^j$ and $u_{fo}^j = u_{fe}^j = \overline{u}_f^j$, are recovered; Eqs. (9) and (10) reveal that the fluid velocities do not vary axially.

2.3. Momentum balances in a slug unit

We can write integral linear momentum balances over the expanding or contracting control volumes representing the slug body, elongated bubble, and liquid film regions to obtain one-dimensional equations for the momentum conservation. Starting with the slug body of unit cell j, and knowing that the liquid velocity does not vary along it, we may write

$$\frac{d}{dt}\left(\rho_l u_{ls}^j A\, l_s^j\right) = \rho_l A\left(u_{ls}^j - u_t^j\right)u_{ls}^j - \rho_l A\left(u_{ls}^j - \dot{\xi}^j\right)u_{ls}^j + \left(P_{s\eta}^j - P_{s\xi}^j\right)A - \tau_s^j \pi d\, l_s^j - \rho_l g A l_s^j \sin\theta^j, \tag{18}$$

where $P_{s\xi}^j$ and $P_{s\eta}^j$ are the pressures at ξ^j and η^j, respectively, on the side of the slug body; both are taken at the level of the pipe axis. Pressure $P_{s\xi}^j$ appears in this equation after integrating the profile $P_{s\xi}^j + \rho_l g(h_{\text{ref}} - \zeta)\cos\theta^j$ over the surface of the pipe cross section at ξ^j,

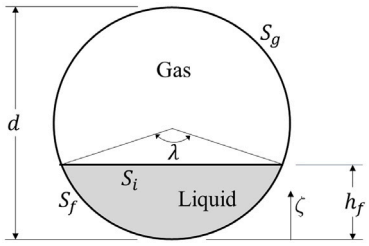

Fig. 2. Pipe cross section in the elongated bubble-film region.

where ζ is a local coordinate running in the cross section at ξ^j from its lowest point, with h_{ref} being set arbitrarily to $d/2$, the level of the pipe axis; the same can be said about $P^j_{s\eta}$. Gravity contributions at each face cancel. The shear stress at the wall in the slug body is denoted by τ^j_s, and g is the acceleration of gravity. Expanding the left-hand side of Eq. (18) and recalling Eq. (3), gives

$$\frac{d}{dt}\left(\rho_l u^j_{ls}\right) = \frac{\left(P^j_{s\eta} - P^j_{s\xi}\right)}{l^j_s} - \tau^j_s \frac{\pi d}{A} - \rho_l g \sin\theta^j. \tag{19}$$

For the elongated bubble, the momentum conservation can be written as

$$\frac{d}{dt}\left(\rho^j_g \alpha^j_g \overline{u}^j_g A\, l^j_f\right) = \rho^j_g \alpha^j_g A \left(u^j_{ge} - \dot{\xi}^{j+1}\right) u^j_{ge} - \rho^j_g \alpha^j_g A \left(u^j_{go} - u^j_t\right) u^j_{go} + \left(P^j_e - P^j_o\right) \alpha^j_g A - \overline{\tau}^j_g S^j_g\, l^j_f - \overline{\tau}^j_i S^j_i\, l^j_f - \rho^j_g \alpha^j_g A\, l^j_f g \sin\theta^j, \tag{20}$$

where P^j_o and P^j_e are the pressures on faces η^j and ξ^{j+1}, respectively, on the side of the elongated bubble-film combined region, respectively, at the level of the gas-liquid interface. In addition, $\overline{\tau}_g$ denotes the average shear stress between the pipe wall and the gas, whilst $\overline{\tau}_i$ is the average shear stress at the elongated bubble-film interface; S_g is the wetted perimeter of the gas, and S_i is the length of the interface within a given pipe cross section (Fig. 2). As in the case of the slug body, to account for hydrostatic pressure variation at a given cross section, we write the pressure, for instance, at η^j, as $P^j_o + \rho_l g \cos\theta^j (h^j_f - \zeta)$ in the liquid film, and as $P^j_o - \rho^j_g g \cos\theta^j (\zeta - h^j_f)$ in the gas bubble. Here, h_f is the liquid film thickness and ζ is a local spatial coordinate defined in the same way as for the analysis of the slug body presented before, and so it is inscribed to a given cross section (see also Fig. 2). A similar pressure profile is considered at ξ^{j+1}, the position of the elongated bubble tail. Integration of these pressure profiles over the surface of the cross section yields the term with pressure difference of Eq. (21), where contributions from $g\cos\theta^j$ from each face cancel since the film thickness is uniform. These contributions, on the other hand, do appear in the surface momentum balances described below. A relationship between the film thickness h_f and the film holdup α_f derived from the geometry in Fig. 2 is given in Appendix C. Expressions for S_g and S_i, as well as the relation between the inclination angle and the arclength coordinates of the front and tail of a slug unit cell are also included there.

With Eqs. (13) and (15), the first two terms on the right-hand side vanish. By expanding the left-hand side of Eq. (21), using Eq. (4), the resulting rearrangement leads to

$$\frac{d}{dt}\left(\rho^j_g \alpha^j_g \overline{u}^j_g\right) = -\frac{\rho^j_g \alpha^j_g}{l^j_f}\left(u^j_t - \dot{\xi}^{j+1}\right)\overline{u}^j_g + \frac{\alpha^j_g\left(P^j_e - P^j_o\right)}{l^j_f} - \frac{\overline{\tau}^j_g S^j_g}{A} - \frac{\overline{\tau}^j_i S^j_i}{A} - \rho^j_g \alpha^j_g g \sin\theta^j, \tag{21}$$

Proceeding in a similar manner as for the elongated bubble, the momentum conservation for the liquid film may be expressed as

$$\frac{d}{dt}\left(\rho_l \alpha^j_f \overline{u}^j_f\right) = -\frac{\rho_l \alpha^j_f}{l^j_f}\left(u^j_t - \dot{\xi}^{j+1}\right)\overline{u}^j_f + \frac{\rho_l \alpha^j_f}{l^j_f}\left(u^j_{fe} - \dot{\xi}^{j+1}\right) u^j_{fe} - \frac{\rho_l \alpha^j_f}{l^j_f}\left(u^j_{fo} - u^j_t\right) u^j_{fo} + \frac{\alpha^j_f\left(P^j_e - P^j_o\right)}{l^j_f} - \overline{\tau}^j_f \frac{S^j_f}{A} + \overline{\tau}^j_i \frac{S^j_i}{A} - \rho^j_l \alpha^j_f g \sin\theta^j, \tag{22}$$

where $\overline{\tau}_f$ is the average shear stress between the liquid film and the pipe wall, and S_f is the film wetted perimeter (see Fig. 2 and Appendix C). The average velocities $\overline{u}_g$ and $\overline{u}_f$ are given, respectively, by Eqs. (11) and (12).

Equations (13)–(16) are mass balances written at surfaces located at ξ^j and η^j, respectively. Similarly, we can write momentum balances at these positions – treated as surfaces of discontinuity – by following, for example, the ideas in section 5.18 of Panton (2013). At position ξ^j, we have

$$P^j_{s\xi} + \rho_l\left(u^j_{ls} - \dot{\xi}^j\right) u^j_{ls} = P^{j-1}_e + \rho_l \alpha^{j-1}_f \left(u^{j-1}_{fe} - \dot{\xi}^j\right) u^{j-1}_{fe} + \rho^{j-1}_g \alpha^{j-1}_g \left(u^{j-1}_{ge} - \dot{\xi}^j\right) u^{j-1}_{ge} + \left(\rho_l \alpha^{j-1}_f \Sigma^{j-1}_f - \rho^{j-1}_g \alpha^{j-1}_g \Sigma^{j-1}_g\right) g\cos\theta^{j-1}, \tag{23}$$

whilst at position η^j, the following momentum balance can be written

$$P^j_{s\eta} + \rho_l\left(u^j_{ls} - u^j_t\right) u^j_{ls} = P^j_o + \rho_l \alpha^j_f \left(u^j_{fo} - u^j_t\right) u^j_{fo} + \rho^j_g \alpha^j_g \left(u^j_{go} - u^j_t\right) u^j_{go} + \left(\rho_l \alpha^j_f \Sigma^j_f - \rho^j_g \alpha^j_g \Sigma^j_g\right) g\cos\theta^j, \tag{24}$$

where

$$\alpha^j_f A \Sigma^j_f = \int_{A^j_f}\left(h^j_f - \zeta\right) dA, \qquad \alpha^j_g A \Sigma^j_g = \int_{A^j_g}\left(\zeta - h^j_f\right) dA. \tag{25}$$

In these expressions, $A^j_f = \alpha^j_f A$ and $A^j_g = \alpha^j_g A$, and ζ denotes the local coordinate shown in Fig. 2. The integrals in Eq. (25) introduce the hydrostatic contribution of the film level that causes gradual pressure variations in the direction orthogonal to the axis of the pipe. Equations (23) and (24) can be further simplified by utilizing Eqs. (13)–(16). The pressure difference resulting from Eq. (23) resembles the acceleration pressure drop sometimes introduced in the literature in a rather heuristic fashion (see, for example, Dukler and Hubbard, 1975). In the model proposed here, this pressure difference arises from a formal momentum balance or "jump law" at a surface at ξ^j.

The average shear stresses at the wall, $\overline{\tau}_g$ and $\overline{\tau}_f$ and at the interface, $\overline{\tau}_i$ are determined by integration of the local shear stresses. These are evaluated, in turn, from the local fluid velocities described in Eqs. (9) and (10), using the closure relationships listed in Appendix A. The wall shear stress in the slug body, τ_s, is computed with velocity u_{ls} and the liquid properties, using the same correlations. In this study, the pipes are considered smooth for the purpose of evaluating the shear stresses. Finally, the density of the gas in the elongated bubble of unit cell j is obtained with the known temperature and the average pressure $(P^j_o + P^j_e)/2$.

In a reference frame translating with the bubble nose, the liquid experiences a gradual contraction when it travels from the slug body to the film region, due to the smooth profile typical of the bubble nose. With this in mind, we modify the pressure difference $P^j_{s\eta} - P^j_o$ in Eq. (24) in a heuristic fashion by introducing the ratio of pressure differences $K_c = (\Delta P)_{\text{gradual}}/(\Delta P)_{\text{sudden}}$. Here, these pressure differences are attained from the Bernoulli (energy) equation with head losses for steady, single-phase flow of a liquid applied to a gradual and sudden contraction, respectively, written for a frame moving with the bubble nose velocity and disregarding changes in potential energy (due to gravity). Following these considerations, for a sudden contraction, the pressure difference may be written as

$$(\Delta P)_{\text{sudden}} = \frac{\rho_l}{2}\left[(u^j_{fo} - u^j_t)^2 - (u^j_{ls} - u^j_t)^2 + K_L (u^j_{fo} - u^j_t)^2\right], \tag{26}$$

where the last term has the usual form for expressing the head losses, with K_L denoting the head loss coefficient for abrupt or sudden contractions. For a gradual contraction, losses are negligible in comparison

Table 1
Loss coefficient for an abrupt contraction.

α_f	0	0.1	0.2	0.3	0.4	0.5	0.6	0.7	0.8	0.9	1
K_L	0.50	0.46	0.41	0.36	0.30	0.24	0.18	0.12	0.06	0.02	0

with a sudden contraction (Street et al., 1996) and so $(\Delta P)_{\text{gradual}}$ is equal to the right-hand side of Eq. (26) without the last term. From these considerations, we obtain

$$K_c = \frac{1-\alpha_f^2}{1-\alpha_f^2+K_L}, \tag{27}$$

where the term $1-\alpha_f^2$ results from the change in the kinetic energy after using Eq. (16) to substitute for $u_{ls}^j - u_t^j$. Using K_c in Eq. (27) to correct the linear momentum exchange in Eq. (24) yields

$$P_{sn}^j - P_o^j = \rho_l K_c \left(u_{ls}^j - u_t^j\right)\left(u_{fo}^j - u_{ls}^j\right) + \left(\rho_l \alpha_f^j \Sigma_f^j - \rho_g^j \alpha_g^j \Sigma_g^j\right) g \cos\theta^j, \tag{28}$$

which has been simplified after employing Eq. (15). The loss coefficient K_L is interpolated from the arrays given in Table 1 (taken from Table 2 in Section 9.9 of Street et al., 1996) using the actual magnitude of α_f for the ratio of cross sectional areas after and before the sudden contraction. We shall use the momentum balance in Eq. (28) instead of Eq. (24). The correction of the latter by means of factor K_c is loosely motivated by the approach implemented by Grigoleto et al. (2021) to obtain an expression for the pressure jump at the slug body front, where a sudden expansion exists as the film is picked up by the following slug body. At the slug body tail (bubble nose plane), those authors neglected any pressure jump. On the other hand, we introduce no correction to the momentum balance at the slug body front of Eq. (23) as it precisely applies to a sudden expansion. Note also that Eq. (23) can be simplified by invoking Eqs. (13) and (14).

3. Conditions at the pipe ends

3.1. Slug initiation at pipe inlet

In this study, we assume that slugs are initiated only at the pipe inlet. The slug unit cells entering the pipe are generated from the mechanistic model described in Section 2 by imposing the steady state condition (i.e., by dropping the time derivatives). To complete the model, we furnish the value of the slug body length. For this purpose, we modify a model recently presented for a horizontal flow by Klinkenberg and Tijsseling (2021), who postulated that the slug body length of the entering slug unit cell obeys a log-normal random distribution with a mean obtained from the slug frequency expression for steady state, namely, $\omega_s = u_t/l_u$. Using $l_u = l_s + l_f$ for the unit cell length, the slug frequency reads

$$\langle l_s/d\rangle_L = \frac{u_t}{\omega_s d\,(1+\mathcal{R})}, \tag{29}$$

where $\mathcal{R}$ is the film length to slug body length ratio; an expression for this ratio can be attained from the relation of the liquid superficial velocity with the amount of liquid in a unit cell passing through a fixed pipe cross section in the steady state slug flow (e.g., Taitel and Barnea, 1990b)

$$\mathcal{R} = \frac{j_l - u_{ls}}{\alpha_f \overline{u}_f - j_l}. \tag{30}$$

For the slug frequency, we follow Klinkenberg and Tijsseling (2021) and apply the correlation by Schulkes (2011). That is,

$$\omega_s = \frac{u_s}{d}\Psi(\lambda_l)\Phi(Re_l)\Theta(\theta_{\text{in}}, Fr), \tag{31}$$

with

$$\Psi(\lambda_l) = 0.016\lambda_l(2+3\lambda_l), \tag{32}$$

$$\Phi(Re_l) = \begin{cases} 12.1\,Re_l^{-0.37}, & Re_l < 4000, \\ 1, & Re_l \geqslant 4000, \end{cases} \tag{33}$$

and

$$\Theta(\theta_{\text{in}}, Fr) = \begin{cases} 1 + 2Fr^{-1}\text{sgn}(\theta_{\text{in}})\sqrt{|\theta_{\text{in}}|}, & |\theta_{\text{in}}| \leqslant 0.17, \\ 1.8Fr^{-1}(0.6 + 2\theta_{\text{in}} - \theta_{\text{in}}^2), & \theta_{\text{in}} > 0.17, \end{cases} \tag{34}$$

where the mixture velocity, $u_s = j_l + j_g$; $\lambda_l = j_l/u_s$ is the non-slip liquid holdup; $Re_l = \rho_l u_s d/\mu_l$ is a liquid Reynolds number, $Fr = j_l/\sqrt{dg\cos\theta_{\text{in}}}$ is the Froude number, and θ_{in} is the pipe inclination angle (in radians) with respect to the horizontal axis at the pipe inlet.

For the standard deviation of the slug body length, Klinkenberg and Tijsseling (2021) used the correlation by Al-Safran et al. (2005) for horizontal flow. Instead, to generalize the approach to inclined flow, based on the review by Fabre and Liné (1992), where they reported that, for horizontal flow, the standard deviation of the slug body length is between 30 and 70% of the mean, and for vertical flow is 20%, we propose the linear interpolation

$$\sigma_L = \left[\hat{\sigma}_{LH}\,\left(1 - \theta_{\text{in}}/(\pi/2)\right) + \hat{\sigma}_{LV}\,\theta_{\text{in}}/(\pi/2)\right]\langle l_s/d\rangle_L\,. \tag{35}$$

Following Fabre and Liné (1992), we set $\hat{\sigma}_{LH} = 0.5$ (average of 0.3 and 0.7) and $\hat{\sigma}_{LV} = 0.2$.

A log-normal probability distribution is specified by two parameters, the mean of logarithmic values, μ_N, and the standard deviation of logarithmic values, σ_N. Their relation with the mean and standard deviation of the log-normal distribution is well-known (e.g., see appendix in Al-Safran et al., 2005). These relationships readily yield

$$\sigma_N^2 = \log\left[1 + \sigma_L^2/\langle l_s/d\rangle_L^2\right], \tag{36}$$

which is then used in computing

$$\mu_N = \log\langle l_s/d\rangle_L - \sigma_N^2/2. \tag{37}$$

With parameters μ_N and σ_N, the log-normal distribution for the slug body length l_s/d with the mean $\langle l_s/d\rangle_L$ and standard deviation σ_L is completely determined, entailing random values of the slug body length.

Finally, we set a lower bound of $4d$ for the slug body length at an initiation. Smaller values may eventually lead to difficulties in the convergence of the numerical solver.

3.2. Outlet conditions

We may identify three stages as the leading slug unit exits the pipe outlet. These depend upon which part of that slug unit cell is either crossing the pipe outlet plane or approaching it. Following the order in which they occur, each of these stages and the various mathematical constraints associated with them are described in the following.

- *Stage 1*: The leading slug body is crossing the plane of the outlet, and its liquid is allowed to leave the pipe (Fig. 3a). The velocity of the slug front is set to zero, $\dot{\xi}^{(1)} = 0$, and the pressure in this location is fixed, $P_{s\xi}^{(1)} = P_{\text{out}}$. Adopting a cautious approach to avoid non-convergence issues, the leading slug body is removed from the system when its length is shorter than a critical value, arbitrarily set here to $2.5\,d$, or the time scale $l_s^{(1)}/u_t^{(1)}$ corresponding to the leading slug body (crossing the outlet plane) is smaller than $d/(j_l + j_g)$. The same criteria are used for the merging of consecutive slug unit cells.
- *Stage 2*: After the leading slug body has left the pipe, the bubble nose translational velocity $u_t^{(1)}$ is set to zero, whilst the gas in the bubble and liquid in the film can cross the plane of the bubble nose (Fig. 3b). In addition, the film velocity at the outlet plane is fixed, such that at the bubble nose the film velocity $u_{fo}^{(1)} = u_{fo}^{(1)*}$ and the pressure $P_o^{(1)} = P_o^{(1)*}$, where $u_{fo}^{(1)*}$ and $P_o^{(1)*}$ denote their

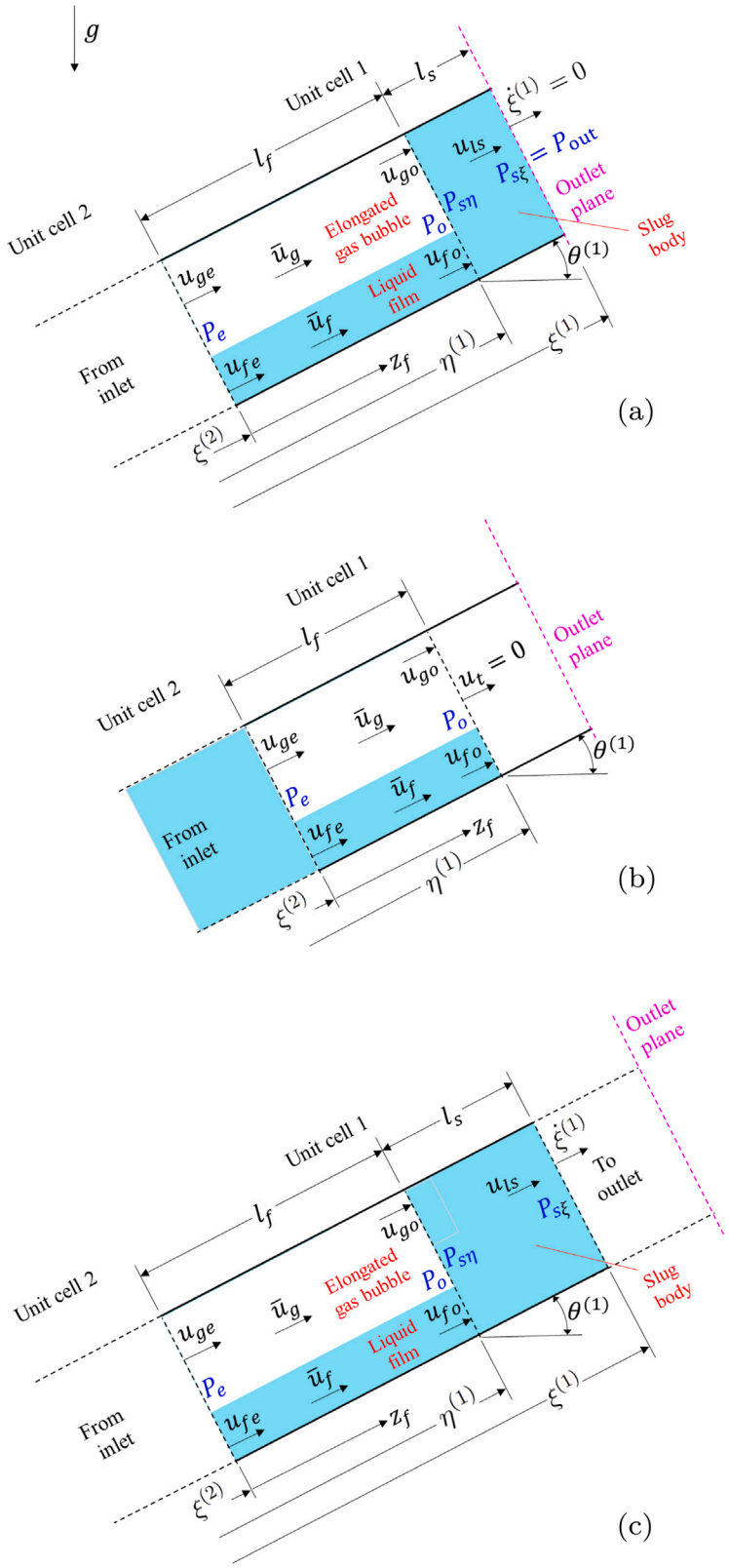

Fig. 3. The three stages of the outlet process.

magnitudes at the instant when the leading slug body left the pipe. Once the film length becomes smaller than the arbitrarily-set small length of $1.5\,d$, the leading film and bubble are removed from the system implying that the entire leading slug unit cell has exited the pipe.

- *Stage 3*: After removing the slug unit cell closest to the outlet, the next slug unit cell becomes the leading one. Its front has yet to reach the outlet (Fig. 3c). In this stage, we impose the condition that the amount of liquid mass crossing the rear boundary of the slug body equals the liquid mass exchange at the front. The other

Table 2
Equations governing the motion of a typical slug unit cell.

Physical meaning	Equation number
Slug front kinematic condition	(1)
Bubble nose kinematic condition	(2)
Mass balance for the elongated bubble	(7)
Mass balance for the liquid film	(8)
Average velocity of the gas in the bubble	(11)
Average velocity of the liquid in the film	(12)
Gas mass balance at slug front	(13)
Liquid mass balance at slug front	(14)
Gas mass balance at bubble nose	(15)
Liquid mass balance at bubble nose	(16)
Volume fraction constraint	(17)
Momentum balance for the slug body	(19)
Momentum balance for the elongated bubble	(21)
Momentum balance for the liquid film	(22)
Momentum balance at slug front	(23)
Momentum balance at bubble nose	(28)
Bubble nose translational velocity	(A.1)
Gas equation of state	Ideal gas law

imposed condition is that the pressure at the slug front changes linearly with the distance to the outlet according to the relation

$$P_{s\xi}^{(1)} = P_{\text{out}} + \frac{(P_{s\xi}^{(1)*} - P_{\text{out}})}{(\xi^{(1)*} - L)}(\xi^{(1)} - L), \tag{38}$$

where $\xi^{(1)*}$ is the arclength coordinate of the slug body front when Stage 3 begins and $P_{s\xi}^{(1)*}$ is the corresponding value of $P_{s\xi}^{(1)}$; $\xi^{(1)}$ is the arclength coordinate of the slug body front at the current time. When the slug body front reaches the outlet, the configuration of Stage 1 is obtained again.

4. Numerical implementation and model validation

4.1. Discretization of the governing equations

For slug unit j, the model presented in this work consists of 18 equations, which are listed in Table 2. It includes the closure for the bubble nose translational velocity, Eq. (A.1) of Appendix A, and the equation of state for the gas density (ideal gas law). The model contains 18 unknowns per slug unit cell. These are $\{P_{s\xi}, \dot{\xi}, \xi, u_{ls}, P_{s\eta}, u_t, \eta, P_o, u_{fo}, u_{go}, \overline{u}_f, \overline{u}_g, \rho_g, P_e, u_{fe}, u_{ge}, \alpha_f, \alpha_g\}$. In addition, the slug body and film lengths are determined from the relations $l_s^j = \xi^j - \eta^j$ and $l_f^j = \eta^j - \xi^{j+1}$, respectively. Note that if one assumes that the pressure in the elongated bubble is uniform, we have $P_o = P_e$, and the number of unknowns per unit cell is reduced by one. Consequently, one of the equations in the system, also per unit cell, must be removed.

We discretize the ordinary differential equations in time using an implicit, first-order backward Euler scheme. For instance, by considering the mass conservation equation for the elongated gas bubble, discretizing Eq. (7) yields

$$\left(\rho_g^{j(n+1)}\alpha_g^{j(n+1)} - \rho_g^{j(n)}\alpha_g^{j(n)}\right) - \Delta t \frac{\rho_g^{j(n+1)}\alpha_g^{j(n+1)}}{l_f^{j(n+1)}}\left(u_{ge}^{j(n+1)} - u_{go}^{j(n+1)}\right) = 0, \tag{39}$$

where the two consecutive time levels n and $n+1$ are separated by the time step Δt. Variables at the time level n $(n+1)$ are known (unknown) and at time level $n+1$ are unknown. In the algebraic expressions of the model, variables are taken at the time level $n+1$. External and internal borders of the unit cells are advanced according to $\xi^{j(n+1)} = \xi^{j(n)} + \Delta t\, \dot{\xi}^{j(n+1)}$ and $\eta^{j(n+1)} = \eta^{j(n)} + \Delta t\, u_t^{j(n+1)}$, whilst the lengths are then obtained from $l_s^{j(n+1)} = \xi^{j(n+1)} - \eta^{j(n+1)}$ and $l_f^{j(n+1)} = \eta^{j(n+1)} - \xi^{j+1(n+1)}$. The inclination angle of the slug unit and liquid-only cells, modelled as straight segments, is related to the arclength positions ξ^j and $\xi^{(j+1)}$, considered at the time level $n+1$, by means of the geometric expression (C.6). The integration of local shear stresses leading to the average shear stresses is carried out using the sixteen-point Gauss–Legendre quadrature (see, e.g., Katsikadelis, 2016, and Moin, 2010).

4.2. Boundary treatment and initial conditions

At the inlet, the gas and liquid superficial velocities, j_g and j_l, respectively, are specified and, initially, the pipe is filled with the liquid, flowing steadily with the velocity j_l. Gas–liquid slug unit cells are created or 'initiated' at the pipe inlet and merging of consecutive unit cells may take place along the pipe. A slug unit cell in a straight pipe element of diameter d and inclination angle equal to that at the pipe inlet is generated using the associated steady-state slug model. This set of equations must be supplemented with a new slug body length, provided by the scheme in Section 3.1, based on the slug frequency, and the steady-state mass balance relating the liquid superficial velocity with the amount of liquid in a slug unit cell passing through a fixed cross section (e.g., see Eq. 5 in Taitel and Barnea, 1990b). The pressure at the new slug body front is that resulting from the liquid-only flow in the pipe with the outlet pressure P_{out}. For the first slug unit, the initial bubble nose translational velocity is determined from Eq. (A.1) neglecting the factor in brackets, and taking $u_{ls}^{(N_l+N_u+1)} = j_l + j_g$, as the inlet mixture velocity. Here, N_l and N_u are the liquid-only and slug unit cells in the system. For subsequent new slug unit cells, the bubble nose velocity is set equal to the velocity of the tail of the preceding slug unit. This bubble nose velocity determines the initial velocity of the unit cell tail. Once the entering slug unit cell has been created, its slug body front coincides with the tail of the preceding cell and the new one evolves according to the model for unsteady flow described here. The slug unsteadiness after its initiation introduces two more unknowns for the next time level, $\dot{\xi}^{(N_l+N_u+1)}$ and $\xi^{(N_l+N_u+1)}$, with three additional equations, namely, (1), (13), and (14), with $j = N_l + N_u + 1$ and $u_{ls}^{(N_l+N_u+1)} = j_l + j_g$. Once the tail of the elongated bubble crosses the pipe inlet, a new unit cell is generated as described.

The liquid-only section initially filling the pipe is modelled by dividing it into a number of N_l control volumes or cells of the same size, considered as straight segments. The initial number of these cells depends on the problem. With no loss of generality, we assume that the borders of these cells move with the velocity of the front of the first slug unit, $\dot{\xi}^{(N_l+1)}$. The exception is the border of the liquid cell coinciding with the pipe exit, where $\dot{\xi}^{(1)} = 0$. Therefore, the length of this cell changes with time. When it becomes smaller than a set value $(2d)$ and there are two or more liquid-only cells in the pipe, this cell is combined with the following one. If only one liquid-only cell remains, it is removed when its length becomes shorter than a very small tolerance $(\ll d)$. We model the flow in the liquid-only cells with a momentum equation similar to that used for the slug body, Eq. (19), with an inclination angle determined as for a slug unit cell. The velocity in the liquid-only cells, which is the same in all these cells due to the liquid incompressibility, is denoted by u_l, being a function of time only. The pressure, denoted as P_l^j, is continuous across the borders between two consecutive liquid-only cells.

At the pipe outlet, we set

$$P_l^{(1)} = P_{\text{out}}, \tag{40}$$

whilst at the cell border between the last liquid cell inside the pipe and the first slug unit cell we enforce the condition

$$u_l = u_{ls}^{(N_l+1)}, \tag{41}$$

where the last expression substitutes for Eq. (14) at the front of the leading slug unit cell. We always keep these constraints in the system of equations. Depending on the stage of the flow at the outlet, one or both constraints become just 'dummy' equations, acting as placeholders. For instance, we keep Eqs. (40) and (41) in the system even if there are no liquid-only cells in the pipe. If this is the case, we simply have $N_l = 0$. If there are liquid-only cells in the pipe, at the front of the leading slug unit, we also enforce the following conditions

$$\dot{\xi}^{(N_l+1)} = u_t^{(N_l+1)}, \tag{42}$$

$$P_l^{(N_l+1)} = P_{s\xi}^{(N_l+1)}, \tag{43}$$

which replace Eqs. (13) and (23), respectively.

With regard to the outlet flow stages described in Section 3.2, in which case there are no liquid-only cells in the pipe ($N_l = 0$), for Stages 1 and 2, instead of Eq. (42), the constraint $\dot{\xi}^{(1)} = 0$ substitutes for Eq. (14). For the later stage, this expression is just a placeholder. For Stages 1 and 2, condition in Eq. (43) still replaces that in Eq. (23). If the outlet flow condition corresponds to Stage 2 in Section 3.2 – the slug body is effectively out of the pipe – we enforce the conditions on $u_{fo}^{(1)}$ and $P_o^{(1)}$ described there as substitutes for Eqs. (16) and (28), respectively, and a null value for $u_t^{(1)}$ instead of the closure relationship, when modelling the leading unit cell. In this case, and to preserve the size and structure of the Jacobian matrix associated with the solution of non-linear equations (see below), we set the placeholders $P_{s\xi}^{(1)} = P_{s\eta}^{(1)}$ and $u_{ls}^{(1)} = u_{ls}^{(1)*}$, where the last term denotes the value available from the previous time level, instead of the momentum equation in the slug body and the gas mass balance condition, Eq. (15), respectively. When the outlet flow condition is that of Stage 3, the slug body front $\xi^{(1)}$ moves, in general, and we impose the condition that the liquid flows entering and leaving the leading slug body are the same, namely, $u_{ls}^{(1)} - \dot{\xi}^{(1)} = \alpha_f^{(1)}(u_{fo}^{(1)} - u_t^{(1)})$. This is applied instead of Eq. (13) when considering the leading slug unit cell. Moreover, Eq. (23) is replaced with Eq. (38) for $P_{s\xi}^{(1)}$.

4.3. Assembling and solving the system of equations

In total, the model comprises $18N_u$ equations for the pipe section containing slug unit cells (two-phase section); $3N_l$ equations for the liquid-only section of the pipe, and 4 boundary conditions, including 3 at the tail of the entering slug unit cell, and 1 at the pipe outlet, given by Eq. (40). Regarding the number of unknowns, from the two-phase section, we have $18N_u$ unknowns plus 2 needed at the tail of the slug unit entering the pipe, $\{\dot{\xi}^{(N_l+N_u+1)}, \xi^{(N_l+N_u+1)}\}$; the liquid-only section contains $3N_l$ unknowns, namely, $\{P_l^j, \dot{\xi}^j, \xi^j\}$, with $1 \leqslant j \leqslant N_l$, plus 2 more, $\{u_l, P_l^{N_l+1}\}$. When two slug unit cells are merged, the ones that follow the resulting cell are renumbered by reducing their indexes by one. Also, more than one pair of cells can be combined at a given time level.

We seek the solution of the fully-implicit system of non-linear equations by means of a non-linear solver provided in Matlab®, which applies a version of the Newton's method. After discretization, by writing the algebraic equations of the model in such a way that their right-hand side is zero, as in Eq. (39), we use the left-hand side to construct a vector of residuals that we pass to the solver. The vector of results available from the previous time step, representing now the values at the time level n, is provided as the initial guess to the non-linear solver. They are nondimensionalized using the liquid and gas densities as density scales; the mixture velocity at the pipe inlet, given by the sum of the gas and liquid inlet superficial velocities, j_g and j_l, respectively, assumed to be known (see below), as the velocity scale; the product $\rho_l(j_l+j_g)^2$, as the pressure scale, and $10\,d$ as the length scale. This initial guess is converted back to a dimensional form to compute the vector of residuals. These residuals are, in turn, nondimensionalized using the same scales.

The Jacobian matrix is computed numerically, employing finite differences with a tolerance of approximately 10^{-6}. Taking advantage of the fact that the model is one-dimensional in space, we arrange the vectors of initial guessed values and of residuals in such a way that the Jacobian is block-diagonal. Then, following the approach in Krasnopolsky and Lukyanov (2018), and to significantly reduce the computational time, we pass to the solver a sparsity pattern containing an array of ones, indicating the nonzero elements of the Jacobian matrix. The number of equations and unknowns in the system and then the size of the Jacobian matrix changes when a cell is removed at the outlet, merged with another, or generated at the pipe inlet.

In most of the simulations in this work, we set a time step of $\Delta t = 5\times10^{-3}$ s. For validation, in selected cases, we use a much smaller time step ($\Delta t = 2\times10^{-3}$ s), obtaining results that do not differ significantly from those computed with the larger time step. Note that Rosa et al. (2015) and Grigoleto et al. (2021) used the time steps of 10^{-3} s and 10^{-4} s, respectively, whilst Vásquez and Avila (2021) used a larger value of 10^{-2} s. We notice that in running our computer codes, the maximum absolute value of the residuals after convergence at a given time step is typically no more than 10^{-7}. The number of iterations needed for convergence in the non-linear solver is usually 2; in a few cases, 3. The exception is at the beginning of a simulation, where up to 8 iterations may be needed. This is likely because of the initial transient associated with the difference in magnitudes between the fluxes inside the pipe and at its inlet, and also because a compressible fluid is being introduced into the dynamic system.

4.4. Scheme for merging of consecutive slug unit cells

In our model, two consecutive slug unit cells are combined or merged into a single cell if, for the second slug unit cell (farther from the outlet) of the pair, either the length of its slug body $l_s < 2.5\,d$ or the time scale $l_s/u_t < d/(j_l+j_g)$. These criteria for merging apply to the second and subsequent slug units in the system, but not to the leading slug body, which is treated as described in Section 3.2. The critical slug body length below which merging of consecutive elongated bubbles happens in a mass conserving manner was set to $0.5\,d$ to $1\,d$ by Nydal and Banerjee (1996), and to $1\,d$ and $0.5\,d$ in the works of Rosa et al. (2015) and Grigoleto et al. (2021), respectively. We acknowledge that our length threshold is somewhat conservative. However, if its value is reduced or the time scale criterion is removed, convergence difficulties may be encountered for some of the flow conditions considered.

Once the above criteria have been satisfied, the merging of slug units follows a semi-conservative approach for mass and momentum that we summarize here. The merging process is assumed to occur instantaneously at a given time level. The calculations of this process are aimed at finding the attributes of the single slug unit cell replacing two consecutive cells whose attributes are known. The found attributes will be used as the initial condition (and initial guess) that enables the solver to advance the solution to the next time level.

Consider the two consecutive slug unit cells that are going to be combined. We denote the slug unit cell closer to the outlet with the superscript '1' and the next one with '2'. By using the parametrization of the pipe axis, $x = x(s), y = y(s)$, we can find the Cartesian coordinates of the points $s = \xi^{(1)}$ and $s = \xi^{(3)}$, where the latter corresponds to the position of the tail of the second unit cell. The arclength coordinates of the front and tail of the new unit cell are $\xi^{(1)}$ and $\xi^{(3)}$, respectively. The length of the straight segment connecting these two points, $l_u^{(a)}$, obtained from their Cartesian coordinates, is the ensuing length of the slug unit cell after merging. Then, its total volume is $l_u^{(a)}A$, where 'a' denotes a quantity of the cell after merging. The inclination angle of the unit cell after merging is also determined from these coordinates. Note that $l_u^{(a)}A \leqslant l_u^{(1)}A + l_u^{(2)}A$, the sum of the volumes of slug units '1' and '2', where the equality holds if the two merging unit cells belong to the same straight pipe element. If unit cell '2' is still entering the pipe and its tail is out, this tail is regarded as moving on a straight segment with the inclination angle of the pipe inlet.

The slug body length after merging is computed assuming that the ratio of the slug body length to the unit cell length after merging is equal to the ratio of the sum of the slug body lengths of cells '1' and '2' to the sum of the lengths of these slug unit cells. This yields

$$l_s^{(a)} = \frac{l_s^{(1)} + l_s^{(2)}}{l_u^{(1)} + l_u^{(2)}} l_u^{(a)}. \tag{44}$$

Then, the film length after merging is $l_f^{(a)} = l_u^{(a)} - l_s^{(a)}$ and the coordinate of the bubble nose is $\eta^{(a)} = \xi^{(1)} - l_s^{(a)}$. We also assume that the film

holdup after merging is given by the length-weighted average of the holdups of the film regions before merging. That is,

$$\alpha_f^{(a)} = \frac{l_f^{(1)}\alpha_f^{(1)} + l_f^{(2)}\alpha_f^{(2)}}{l_f^{(1)} + l_f^{(2)}}, \tag{45}$$

with the void fraction of the elongated bubble after merging given by $\alpha_g^{(a)} = 1 - \alpha_f^{(a)}$. The velocity of the liquid in the slug body, $u_{ls}^{(a)}$, the average velocity of the liquid in the film, $\overline{u}_f^{(a)}$, and of the gas in the elongated bubble, $\overline{u}_g^{(a)}$, are obtained by enforcing the equality of the linear momenta before and after merging. That is,

$$m_s^{(a)}u_{ls}^{(a)} = m_s^{(1)}u_{ls}^{(1)} + m_s^{(2)}u_{ls}^{(2)}, \tag{46}$$

$$m_f^{(a)}\overline{u}_f^{(a)} = m_f^{(1)}\overline{u}_f^{(1)} + m_f^{(2)}\overline{u}_f^{(2)}, \tag{47}$$

$$m_g^{(a)}\overline{u}_g^{(a)} = m_g^{(1)}\overline{u}_g^{(1)} + m_g^{(2)}\overline{u}_g^{(2)}, \tag{48}$$

where the masses of liquid in the slug body and film of unit cell '1' are $m_s^{(1)} = \rho_l l_s^{(1)} A$, and $m_f^{(1)} = \rho_l \alpha_f^{(1)} l_f^{(1)} A$, respectively, and the mass of the gas in the elongated bubble is $m_g^{(1)} = \rho_g^{(1)} \alpha_g^{(1)} l_f^{(1)} A$. Analogous expressions are employed for quantities in unit cell '2'. After merging, for the liquid, $m_s^{(a)} = \rho_l l_s^{(a)} A$ and $m_f^{(a)} = \rho_l \alpha_f^{(a)} l_f^{(a)} A$ and, for the gas, its mass is conserved, hence $m_g^{(a)} = m_g^{(1)} + m_g^{(2)}$.

For the gas density, after merging, we have $\rho_g^{(a)} = m_g^{(a)}/(\alpha_g^{(a)} l_f^{(a)} A)$. Initial guesses for the remaining variables for the next time step are given by $P_{s\xi}^{(a)} = P_{s\xi}^{(1)}$, $P_{sn}^{(a)} = P_{sn}^{(1)}$, $P_o^{(a)} = P_o^{(1)}$, $u_{fo}^{(a)} = u_{fo}^{(1)}$, $u_{go}^{(a)} = u_{go}^{(1)}$, $u_{fe}^{(a)} = u_{fe}^{(2)}$, $u_{ge}^{(a)} = u_{ge}^{(2)}$, and $P_e^{(a)} = P_e^{(2)}$. This completes the computation of the attributes of the ensuing slug unit cell after merging; they are passed to the solver to find the flow field at the next time level.

Since the liquid is incompressible and, in general, the volume of the slug cell after merging is smaller than the sum of the volumes of the slug cells before merging, to avoid situations that may cause spurious results or even halt the execution of a simulation, the proposed merging scheme does not conserve the mass of the liquid. $m_l^{(1,2)} = m_s^{(1)} + m_s^{(2)} + m_f^{(1)} + m_f^{(2)}$ and $m_l^{(a)} = m_s^{(a)} + m_f^{(a)}$, the mass of liquid removed after the merging of two unit cells is $m_l^{(1,2)} - m_l^{(a)}$. If the two slug units being merged are in the same straight pipe element, the mass removed after their merging is zero. Nevertheless, for various cases considered, the total mass of liquid artificially removed from the system due to cells merging during the entire duration of the simulation was insignificant in comparison to the total mass of liquid introduced through the pipe inlet in the same period, or to the liquid mass filling the pipe at the beginning of the simulation.

In summary, when two consecutive slug unit cells merge, the algorithm for this process is as follows. The arclength coordinates of the front and tail of the new slug unit cell are given by $s = \xi^{(1)}$ and $s = \xi^{(3)}$, respectively, which, in turn, determine their corresponding Cartesian coordinates from the riser profile equation. The length of the straight segment connecting the front and tail is $l_u^{(a)}$. Next, the slug body length, $l_s^{(a)}$, of the new slug unit is computed from Eq. (44), so that the film length is $l_f^{(a)} = l_u^{(a)} - l_s^{(a)}$ and the coordinate of the bubble nose becomes $\eta^{(a)} = \xi^{(a)} - l_s^{(a)}$. Then, the new slug unit's film holdup, $\alpha_f^{(a)}$, results from Eq. (45), and the void fraction is $\alpha_g^{(a)} = 1 - \alpha_f^{(a)}$. By conserving the mass of the gas before and after merging, void fraction $\alpha_g^{(a)}$, together with the volume of the elongated bubble-film region, $l_f^{(a)} A$, give the gas density in the new elongated bubble, $\rho_g^{(a)}$. Next, the velocities $u_{ls}^{(a)}$, $\overline{u}_f^{(a)}$, and $\overline{u}_g^{(a)}$, are given by the linear momentum relationships, Eqs. (46), (47), and (48). Finally, initial guesses for the rest of the variables of the new slug unit cell are provided by the values already stored for cells '1' or '2', depending on the position in the new slug unit (slug body or elongated bubble-film tail).

4.5. Validation with experimental data of straight pipes

Since experimental data for rigid catenary curved pipes transporting slug flow are unavailable in the literature, we evaluate the performance of the proposed model by comparing its predictions with experimental measurements for several variables, including the average liquid holdup and pressure gradient, from the works of Felizola (1992) and Hernandez-Perez (2007) on steady gas–liquid slug flows in straight pipes. From the former, we extract data for upward flow in pipes of various inclinations, whilst from the latter we consider the horizontal flow. We also compare predictions versus measurements for the bubble nose translational velocity, slug frequency, and ratio of the film length to slug body length. The experimental conditions of these two studies corresponding to the points included in the comparison are listed in Table 3. The values of the bubble nose translational velocity, the slug frequency, and the film length-to-slug body length ratio are determined at the same location as the average liquid holdup.

Table 3
Conditions used in the simulations of the experimental runs.

	Felizola (1992)	Hernandez-Perez (2007)
d (mm)	50.8	38
L (m)	15.24	6
Inclination (°)	10, 20, 40, 50, 60	0
Gas–liquid	Air–kerosene	Air–water
Number of experimental data points	23	8
Gas superficial velocities (m/s)	0.4–2.02	0.122–0.968
Liquid superficial velocities (m/s)	0.05–0.56	0.2–0.73
Pressure[a] (kPa)	208–255.4	101.3
Temperature (°C)	21.9–37.4	20
Gas specific constant (J kg^{-1} K^{-1})	287.058	287.058
Gas dynamic viscosity (Pa s)	1.83×10^{-5}–1.90×10^{-5}	1.80×10^{-5}
Liquid density (kg m^{-3})	$824.14 - 0.6814\,T$[b]	1000
Liquid dynamic viscosity (Pa s)	$\exp(-6.114 - 0.01365\,T)$[b]	10^{-3}
Holdup 'probe' position[c] (m)	11.1252	4.90
1st pressure 'probe' position[c] (m)	0.0127	4.75
2nd pressure 'probe' position[c] (m)	12.2254	5.515

[a]Set as the outlet pressure.
[b]Temperature T in °C
[c]Distance from the pipe inlet.

The average liquid holdup is computed as the length-weighted average of the holdup in the slug body and the film holdup corresponding to the slug unit cell passing through a fixed position in the pipe. The pressure gradient is obtained as the difference of the two pressure values computed simultaneously at two fixed locations along the pipes divided by the distance between them. The locations of these points, which we call 'probes', are given in Table 3. In the case of Felizola's experiments, the distances are obtained from their drawings, although the exact positioning of the actual pressure probes is not known precisely. As for the experiments by Hernandez-Perez (2007), actual known distances are adopted to replicate their experimental set-up.

Fig. 4 shows the comparison of experimental data for the average holdup and pressure gradient values for gas–liquid slug flows in straight pipes with various inclinations. If we denote by ϑ_{meas} the measured value of a physical quantity in an experiment and by ϑ_{pred} its corresponding model prediction, we define the relative error in absolute value as $e_i = |(\vartheta_{\text{pred},i} - \vartheta_{\text{meas},i})/\vartheta_{\text{meas},i}|$ for the experimental run i. For the average holdup (holdup in a slug unit cell), the average of the relative errors in absolute value for all the data is 16.34% (10.86%), where the standard deviations are in parentheses. With the data from Felizola (1992), it is 18.61% (11.05%). With the data from Hernandez-Perez (2007), it is 9.80% (7.49%). For the pressure gradient, the average of the relative errors in absolute value is 55.33% (30.22%) for all the data. Comparing predictions with the data by Felizola (1992) results in an average value of the errors of 60.62% (30.07%), whilst with the data by Hernandez-Perez (2007), the average value is 40.11% (26.75%). In Fig. 5, we compare measurements with model predictions for the bubble nose translational velocity, slug frequency, and film-to-slug body length ratio. For the translational velocity, the average of the relative errors in absolute value for all the data is 10.20% (7.97%); for the data from Felizola (1992) is 9.34% (8.10%), whilst for Hernandez-Perez's (2007) data is 12.68% (7.53%). In the case of the

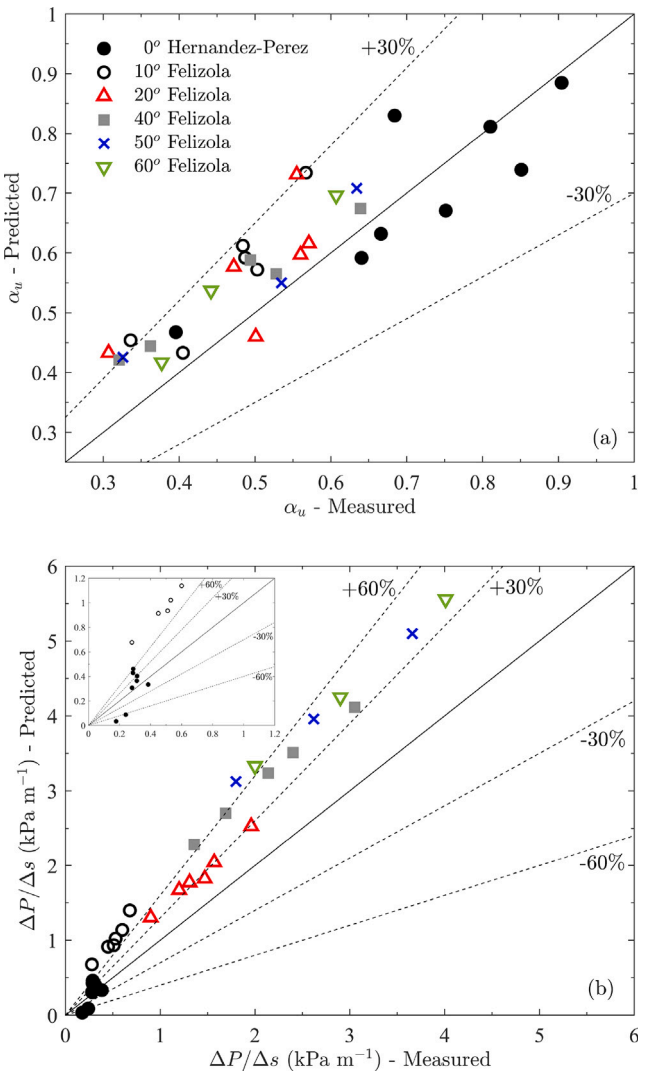

Fig. 4. Comparison of measured and predicted (a) average holdup and (b) pressure gradient for horizontal and inclined-upward gas–liquid flow in straight pipes. Inclination angles range from 0° to 60°.

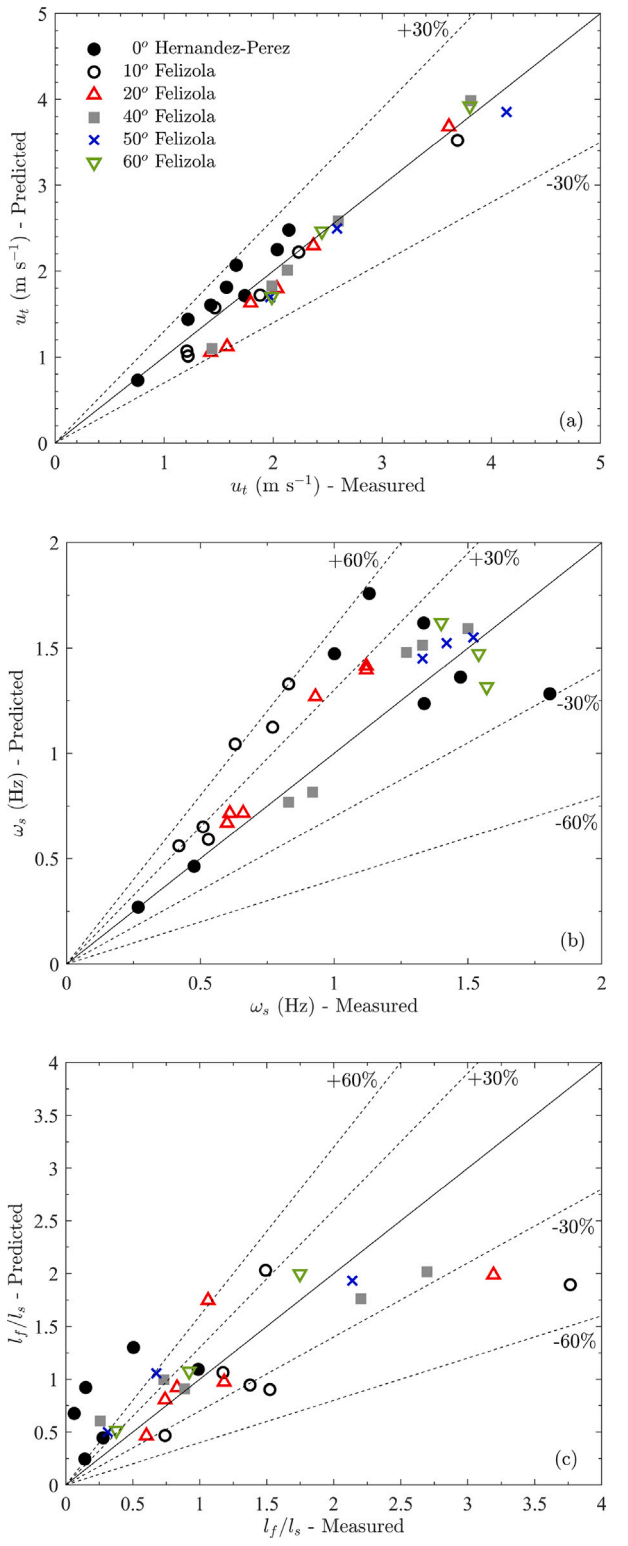

Fig. 5. Comparison of measured and predicted (a) bubble nose translational velocity, (b) slug frequency, and (c) film-to-slug body length ratio for horizontal and inclined-upward gas–liquid flow in straight pipes. Inclination angles range from 0° to 60°.

slug frequency, for all the data the average error is 20.99% (17.89%); for Felizola's (1992) data is 20.83% (17.26%), and for Hernandez-Perez's (2007) is 21.44% (20.85%). For the film length-to-slug body length ratio, the average of the relative errors in absolute value for all the data is extremely high, 88.75% (195.58%), due to the presence of two measurements (Hernandez-Perez's, 2007, data for horizontal flow) where, uncharacteristically, $l_f/l_s \lesssim 0.15$ for values of the gas superficial velocity for which much higher ratios are expected — see Fig. 5(c). Considering these two points as outliers, discarding them results in an average value of the errors of 39.96% (36.37%). For the data from Felizola (1992), the average value of the errors is 33.83% (28.13%), whilst for Hernandez-Perez's (2007) is 75.19% (60.98%) — with the two outliers, the average value of the errors was about four times this value. It should be noted that Hernandez-Perez (2007) only reported the ratio of the slug body length-to-film length for a liquid superficial velocity of 0.73 m s^{-1}, which thus removes two points from the original list of eight points (see Table 3).

The performance of the model with respect to these data set is limited especially for the pressure gradient. The tendency is to over-predict this quantity. This trend might be influenced by the lack of gas in the slug body. For instance, values of gas void fraction between 0.45 to 0.25 in the slug body, which are not negligible, were reported by Felizola (1992). Therefore, a path for improvement may be considering aerated slug bodies, where the gas is in the form of small bubbles that may slip with respect to the liquid. This can significantly reduce the

pressure gradient throughout the slug body, and hence decrease the difference with the experimental data. On the other hand, having gas in the slug bodies may reduce the length of the film region, which may contribute to rise the pressure gradient. Also, a different treatment of the momentum exchange at the bubble nose section may improve the model's predictive capabilities.

5. Unsteady slug flow in catenary risers

In this section, simulations based on the present one-dimensional mechanistic model are performed to track an unsteady gas–liquid slug flow in a curved inclined pipe with a catenary shape and high aspect ratio. The catenary configuration is applicable to a deep-water riser pipe conveying hydrocarbon fluids from the seabed to the sea surface platform. The equation describing the catenary profile in the Cartesian coordinate system is (see Fig. 1)

$$y = (1/K_0)\cosh\left(K_0 x + A_0\right) + B_0, \tag{49}$$

in which the coordinate x can be written as a function of the arclength s as follows

$$x = (1/K_0)\sinh^{-1}\left(K_0 s + C_0\right) - A_0/K_0, \tag{50}$$

where $B_0 = -(1/K_0)\cosh A_0$ and $C_0 = \sinh A_0$, so that when $s = 0$, $x = y = 0$.

For the base case, we consider a long catenary riser of length $L = 600$ m, with horizontal and vertical projections of 503.80 m and 290.87 m, respectively, and an inclination angle at the inlet of 1.86°. From these projections, the chord angle of the catenary results in 30°. To model this geometry, we have $K_0 = 1.972 \times 10^{-3}$ m^{-1} and $A_0 = 3.247 \times 10^{-2}$ in Eqs. (49) and (50). At the outlet (riser top), the catenary has an inclination angle of 50.56° . The inner diameter of this catenary riser is set to be 0.254 m so that its aspect ratio is $L/d = 2362.2$. The dimensions of this catenary are in the order of those of actual curved risers encountered offshore.

With respect to the flow conditions, the outlet pressure is set to be atmospheric, 101.3 kPa and the temperature of the flow everywhere along the pipe is 15°C. For the fluids, we follow Chatjigeorgiou (2017) by considering the methane gas with a specific gas constant of 518.28 J kg^{-1} K^{-1}, used in the ideal gas law, and a dynamic viscosity of 1.090×10^{-5} Pa s, and considering an API 48 crude oil with the liquid density of 790 kg m^{-3} and a dynamic viscosity of 3.002×10^{-3} Pa s.

5.1. Effect of superficial velocities

First, we examine the effect of different combinations of liquid and gas superficial velocities in the one-dimensional flow field for the 600 m-long catenary pipe. These combinations are formed with the values $j_l = \{0.2, 2\}$ m s^{-1} and $j_g = \{0.6, 1, 2\}$ m s^{-1}, of the same order of the combination of superficial velocities used by Chatjigeorgiou (2017) considering a marine riser carrying a steady slug flow. We describe the flow field by means of the profiles of pressure, liquid holdup, and gas–liquid actual velocities inside the riser, amongst other variables. To the best of our knowledge, there are no flow pattern maps available in the literature for upward gas–liquid flow in curved pipes (pipes with variable inclination). We are aware, for instance, of the collection of flow pattern maps compiled in the book by Shoham (2006) for upward gas–liquid flow in straight pipes with inclinations from horizontal to vertical, showing that as the inclination angle increases from the horizontal position, the slug flow region becomes dominant, and the stratified flow region significantly shrinks until disappearing.

In Fig. 6, we show the contour plots of absolute pressure for the entire pipe length and for a time of $0 \leqslant t \leqslant 1400$ s, for four combinations of liquid and gas superficial velocities. Case (a) is for $j_l = 2$ m s^{-1} and $j_g = 2$ m s^{-1}, whilst cases (b), (c), and (d) have fixed liquid superficial velocity, $j_l = 0.2$ m s^{-1}, and increasing gas-to-oil superficial velocity ratio, GOR $= j_g/j_l$, of 3, 5, and 10, respectively. Fig. 6(a) shows an initial transient, lasting about 100 s and characterized by a large pressure peak. This transient results from a jump in the velocity at the inlet section from that of the liquid inside the pipe, 2 m s^{-1}, and that of the first slug body generated at the initial instant, 4 m s^{-1}. It is also affected by the compressibility of the gas being injected. After this transient, the pressure contours depict a relatively steady behaviour, with fluctuations resulting from the randomness of the slug initiation process at the inlet.

Fig. 6(b) shows that the initial pressure transient lasts longer (about 200 s) than for case (a) and with a lower peak value. The duration of this transient decreases as GOR increases. After the initial transient, Fig. 6(b), (c), and (d), depict fluctuations over the entire period considered, with very noticeable contrasts in the amplitudes. By the pipe inlet, the amplitudes of these fluctuations appear to increase with GOR.

By using the continuous wavelet transform, the time-varying frequencies of absolute pressure (ω_P) in Fig. 6 are presented in Fig. 7 for the selected five locations (inlet, $s = 0.25L$, $s = 0.50L$, $s = 0.75L$, and near the outlet, $s = 0.975L$, or $60\,d$ from the outlet) along the curved riser and for the time interval $t = 400 - 1400$ s. The power spectral densities of the wavelets have been normalized by the maximum values such that the largest peaks are unity, as shown by the limit of the contour colour band. For the high values of both j_l and j_g of 2 m s^{-1}, Fig. 7(a) reveals high modulations of ω_P at the five locations, suggesting the greatest space–time fluctuations of pressure. It is also worth remarking the intermittent switching of the predominant frequencies at different times and locations. For the cases of lower $j_l = 0.2$ m s^{-1} with greater $j_g = 0.6$ (Fig. 7b), 1 (Fig. 7c) and 2 (Fig. 7d) m s^{-1}, which show similar pressure contour patterns in Fig. 6, the amplitude modulations as well as the spatial fluctuations of ω_P are enhanced when the slug flow travels from the inlet towards the outlet as well as when increasing j_g. This highlights the greater slug flow intermittency with the increased flow-transporting distance and GOR. Overall, the predominant ω_P values are within the first 0.5 Hz, consistent with the results of slug frequencies presented in the following.

The spatio-temporal evolutions of the liquid holdup and liquid–gas velocities are presented in Fig. 8 for $j_l = 2$ m s^{-1}, $j_g = 2$ m s^{-1} (figures on the left) and $j_l = 0.2$ m s^{-1}, $j_g = 2$ m s^{-1} (figures on the right) for the time interval 850 s $\leqslant t \leqslant$ 900 s. With the same value of j_g, for the first pair of superficial velocities, GOR = 1, whilst for the second pair, GOR = 10. Figs. 8(a) and (b), for the liquid holdup, show the length variation of the slug bodies and film-bubble regions arising from the random slug initiation. Because there is no gas in the slug bodies, the gas in an elongated bubble at initiation remains in that bubble for the entire life of the slug unit cell. Only when two slug units merge, does the gas in a bubble combines with that in another. At any given time, the size of the bubbles increases towards the pipe outlet, due to the decreasing pressure. Case (b), with the largest GOR, exhibits longer elongated bubble-film regions and larger slug bodies than case (a), with the smallest GOR. Consequently, a greater number of slug unit cells are needed to fill the pipe for case (a) than for case (b).

Regarding the contour plots of the *in situ* or actual liquid velocity in the slug bodies and film regions of Figs. 8(c) and (d), we note that the reversed flow, with a negative velocity, dominates in the film regions (dark colours), and its magnitude increases towards the outlet due to the higher inclination. On the other hand, the velocity in the slug bodies varies much lesser than in the film (light colours); its magnitude nevertheless suddenly surges near the outlet in some instances. For the actual gas velocity, Figs. 8(e) and (f) show that it increases significantly as the bubble approaches the pipe outlet, following the increase in the inclination angle and the reduction in pressure. Recall that, according to the model, the gas velocity varies linearly inside an elongated bubble.

In Fig. 9, we present the average values over time and, with error bars, the corresponding standard deviations of relevant slug flow variables at five positions along the 600 m-long catenary riser for several pairs of superficial velocities. Here, the distances are measured from the

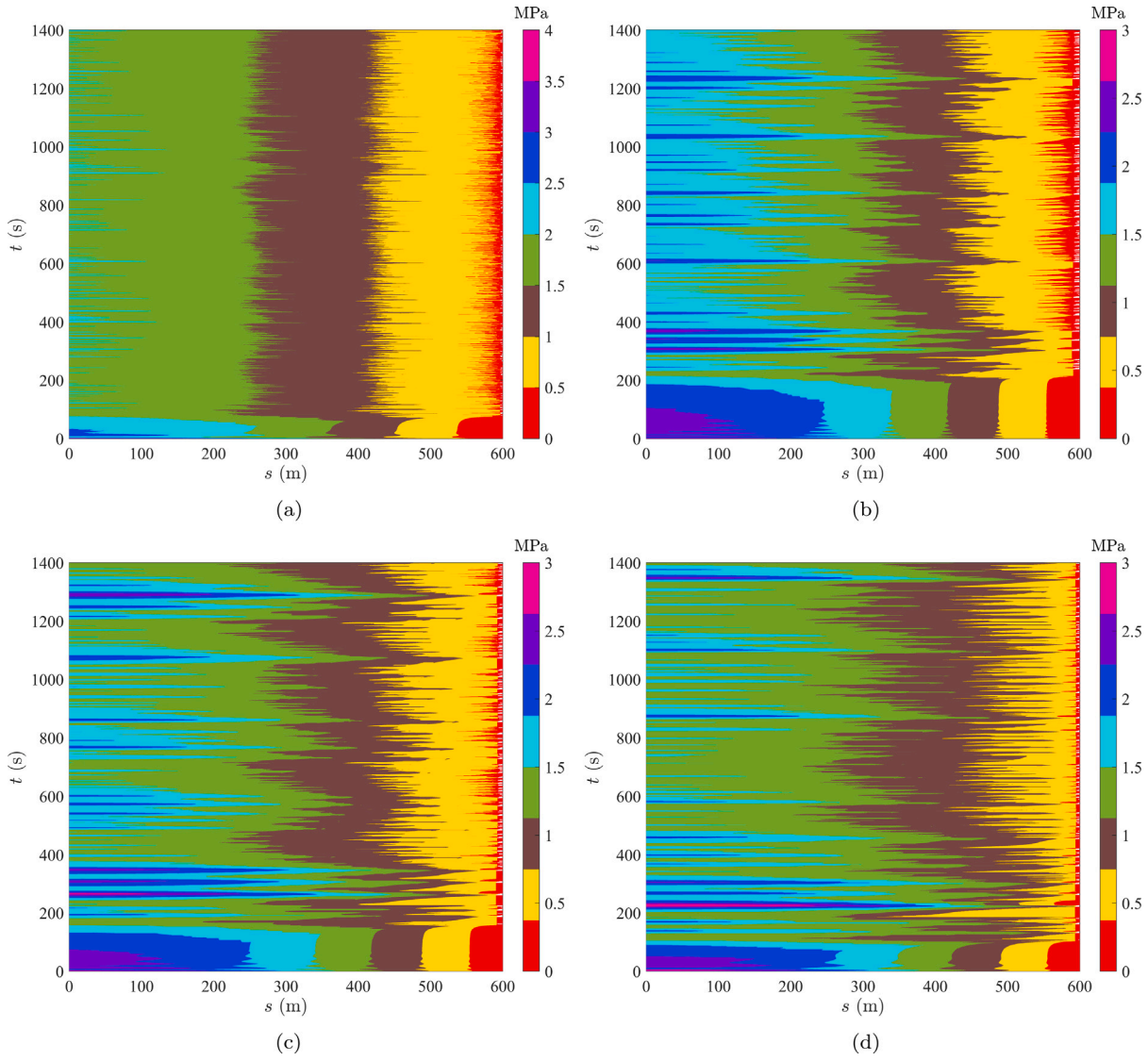

Fig. 6. Contour plots of absolute pressure for the 600 m-long catenary riser and (a) $j_l = 2$ m s^{-1}, $j_g = 2$ m s^{-1}, (b) $j_l = 0.2$ m s^{-1}, $j_g = 0.6$ m s^{-1}, (c) $j_l = 0.2$ m s^{-1}, $j_g = 1$ m s^{-1}, and (d) $j_l = 0.2$ m s^{-1}, $j_g = 2$ m s^{-1}.

inlet. The position 'near the outlet' corresponds to $60d$ from the outlet. The variables included in this figure are the slug body and liquid film dimensionless lengths, l_s/d and l_f/d; the slug front and bubble nose translational velocities, $\dot{\xi}$ and u_t; the slug frequency, ω_s; the velocity of the liquid in the slug body, u_{ls}; the average velocity of the liquid in the film, $\overline{u}_f$; the average slug unit liquid holdup, α_u; the liquid film holdup, α_f, and the pressure gradient, $\Delta P/\Delta s$. This gradient is computed using the pressure difference and the length between corresponding positions in two consecutive slug unit cells ($\Delta P = P_1 - P_2$, where position '1' is closer to the inlet than position '2'). Focusing first on the case of $j_l = 2$ m s^{-1} and $j_g = 2$ m s^{-1}, we note that the mean values of the slug body and film lengths, slug front and bubble nose translational velocities, slug liquid and film (the negative of their values) velocities, and pressure gradient increase as the outlet is approached. The mean of the frequency decreases. The fact that the slug frequency exhibits a decreasing trend indicates that the rise in the slug body and film lengths, which together compose the unit cell length, dominates over the increase in the translational velocity. Fig. 9 also shows that, for $j_l = 2$ m s^{-1} and $j_g = 2$ m s^{-1}, the mean of the average unit cell and film holdups vary moderately. From the values listed, the minimum occurs at $0.75L$ of the pipe inlet. Note also that the slug front and bubble nose velocities have similar mean values except for the location near the outlet. There, the former is smaller than the latter. When the location where the various quantities are recorded lies within the front and tail of the leading slug body and its slug front reaches the outlet, the velocity of the front becomes zero, which affects the statistics.

In Fig. 10, we plot the probability density functions for several slug flow variables at the same five locations used in Fig. 9 for $j_l = 2$ m s^{-1} and $j_g = 2$ m s^{-1}. The area under the curve in each of these figures equals one, and the wider the range in the horizontal axis, the shorter the maximum value reached by the curve. At the inlet, the slug body length and the slug frequency follow a log-normal distribution, as expected. The film length also exhibits this distribution. At the outlet, the curve for the pressure shows more than one peak, which is likely the result of the modelling of the various stages of the outlet process.

For most of the cases, the physical time simulated was $0 \leqslant t \leqslant 2700$ s. The maximum time was reduced to 1435 s for the case of $j_l = 0.2$ m s^{-1} and $j_g = 1$ m s^{-1}. As a reference, for $j_l = 2$ m s^{-1} and $j_g = 2$ m s^{-1} (GOR=1), for the entire simulated period, 1518 slug unit cells were initiated, 764 left the pipe, and there were 723 merging events; 31 cells were inside the pipe when the simulation ended. The sum of the last three amounts equals the number of unit cells initiated. For the same period, the corresponding quantities for the case of $j_l = 0.2$ m s^{-1} and $j_g = 2$ m s^{-1} (GOR=10) were 291, 265, 12, and 14.

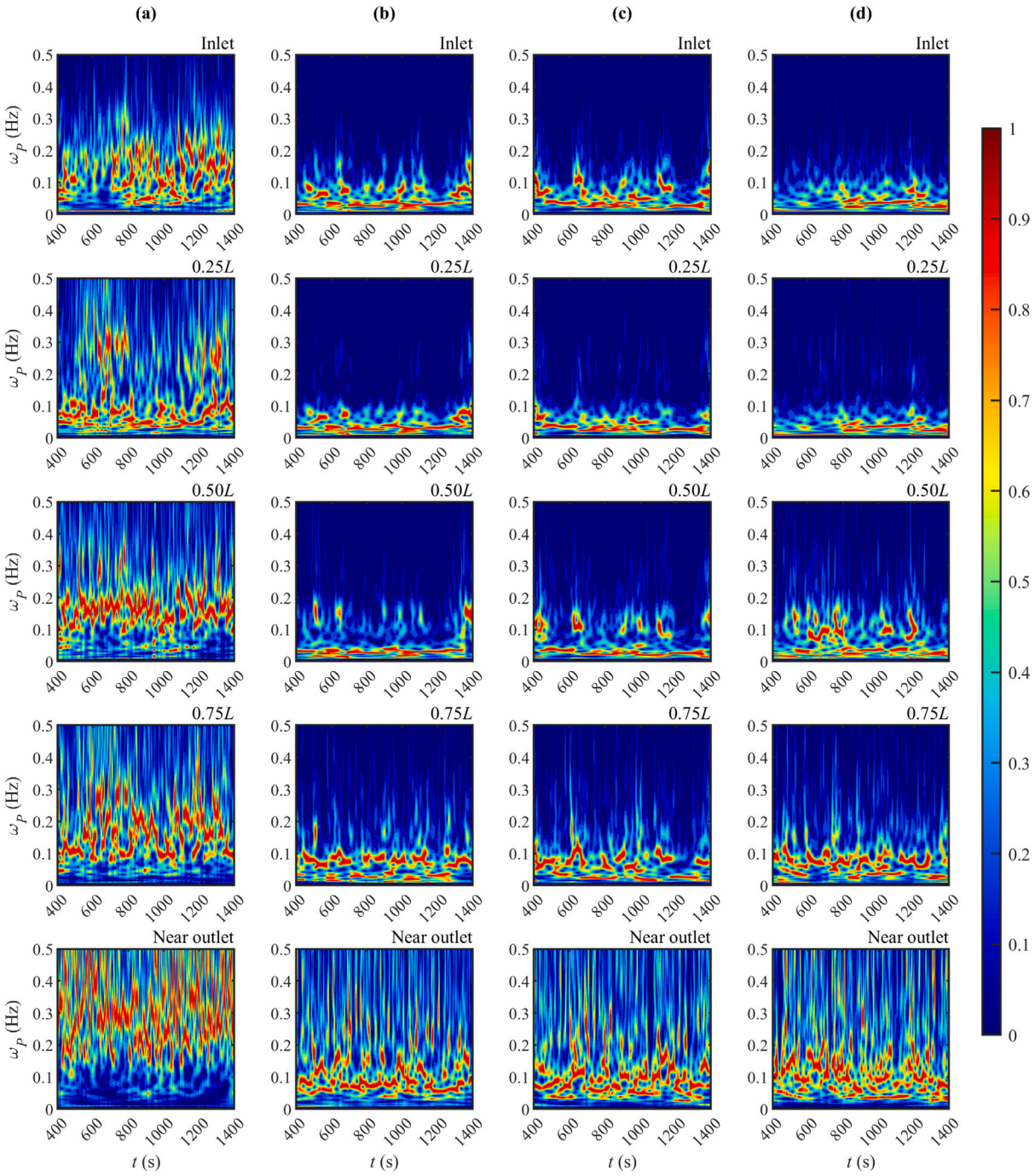

Fig. 7. Wavelet-based frequency plots of absolute pressure in Fig. 6 at specific locations of the 600 m-long catenary riser: (a) $j_l = 2\ \mathrm{m\,s^{-1}}$, $j_g = 2\ \mathrm{m\,s^{-1}}$, (b) $j_l = 0.2\ \mathrm{m\,s^{-1}}$, $j_g = 0.6\ \mathrm{m\,s^{-1}}$, (c) $j_l = 0.2\ \mathrm{m\,s^{-1}}$, $j_g = 1\ \mathrm{m\,s^{-1}}$, and (d) $j_l = 0.2\ \mathrm{m\,s^{-1}}$, $j_g = 2\ \mathrm{m\,s^{-1}}$. The location 'near the outlet' corresponds to $0.975L$.

To examine the effect of varying the superficial velocities on the slug flow dynamics in the 600 m-long catenary riser, we reduce j_g from $2\ \mathrm{m\,s^{-1}}$ to $0.6\ \mathrm{m\,s^{-1}}$ and $1\ \mathrm{m\,s^{-1}}$, while keep $j_l = 2\ \mathrm{m\,s^{-1}}$; hence, GOR $\leqslant 1$. The results are also plotted in Fig. 9. In both cases, the trends for the mean values are similar to those for $j_g = 2\ \mathrm{m\,s^{-1}}$ as the observation point changes from the inlet to the outlet. Regarding the slug body and film lengths, for $j_g = 0.6\ \mathrm{m\,s^{-1}}$, the mean of l_s/d is greater than that of l_f/d at all the stations. For $j_g = 1\ \mathrm{m\,s^{-1}}$, this also holds except for the station near the outlet. For $j_g = 2\ \mathrm{m\,s^{-1}}$, the mean of l_f/d is larger than that of l_s/d for the last two stations. It is somewhat remarkable that the mean of the average film velocity and the film holdup have similar values for the three cases where $j_l = 2\ \mathrm{m\,s^{-1}}$ (i.e. GOR $\leqslant 1$) in every station. The mean of the average slug unit liquid holdup increases as GOR decreases. The same occurs for the mean of the pressure gradient at $0.25L$, $0.50L$, and $0.75L$; the opposite is observed near the outlet.

Considering cases with GOR > 1, we set $j_l = 0.2\ \mathrm{m\,s^{-1}}$ whilst $j_g = 0.6, 1$ and $2\ \mathrm{m\,s^{-1}}$. For these cases, the mean values of the flow variables follow qualitatively the trends reported for the flow with $j_l = j_g = 2\ \mathrm{m\,s^{-1}}$. We notice that for $j_l = 0.2\ \mathrm{m\,s^{-1}}$ and $j_g = 2\ \mathrm{m\,s^{-1}}$, the mean of l_f/d is larger than the mean of l_s/d at every position considered, due to the large GOR of 10. When j_g decreases to $1\ \mathrm{m\,s^{-1}}$, at the inlet, the mean of l_f/d is again larger but they tend to become equal as the outlet is approached. This trend also occurs for the smallest value of j_g, $0.6\ \mathrm{m\,s^{-1}}$, except that at the inlet, the mean of l_f/d is shorter than that of l_s/d. Another feature is that the mean of the slug frequency is significantly smaller for these three cases than for the cases with

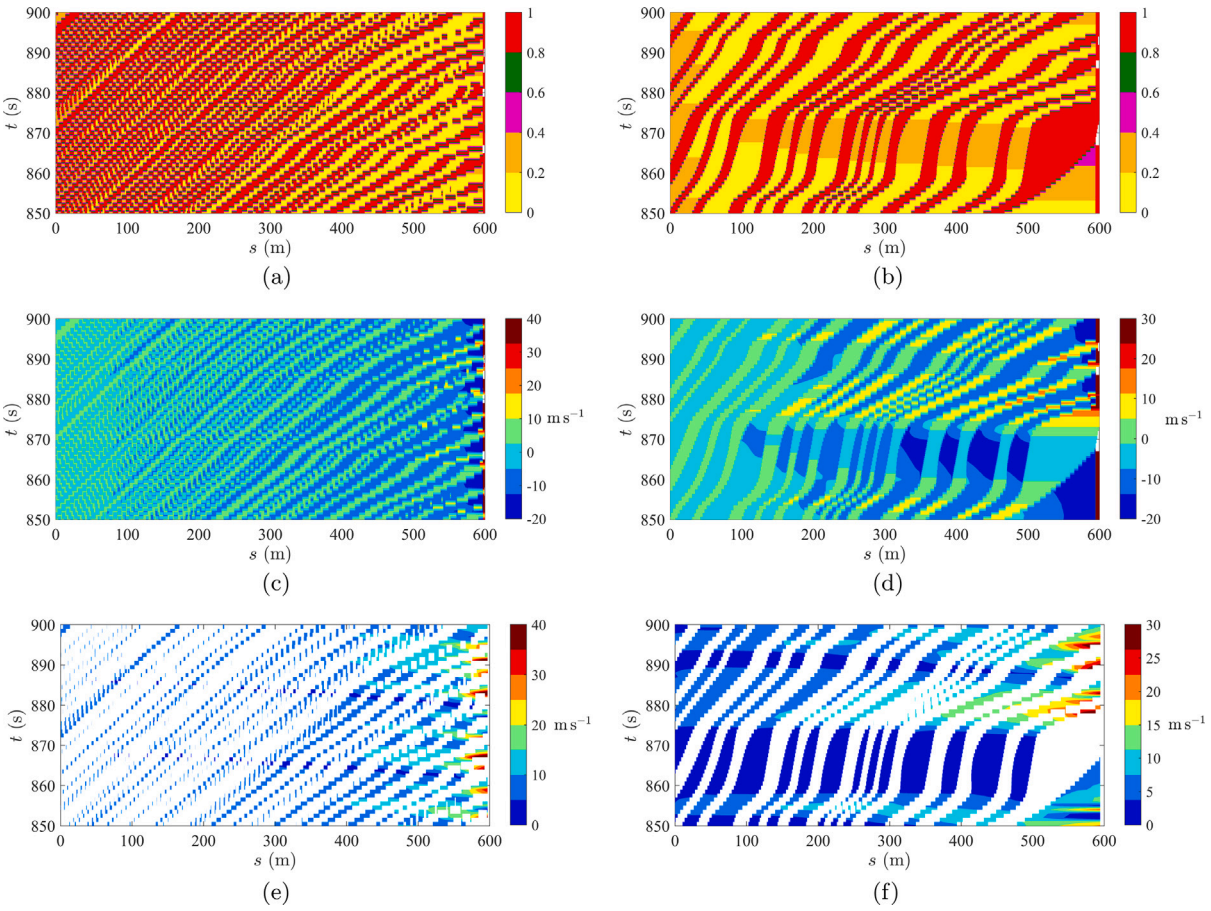

Fig. 8. Contour plots of (a) and (b) liquid holdup, (c) and (d) liquid velocity, and (e) and (f) gas velocity for the catenary riser. The figures on the left are for $j_l = 2\ \mathrm{m\,s^{-1}}$ and $j_g = 2\ \mathrm{m\,s^{-1}}$ and those on the right for $j_l = 0.2\ \mathrm{m\,s^{-1}}$ and $j_g = 2\ \mathrm{m\,s^{-1}}$.

$j_l = 2\ \mathrm{m\,s^{-1}}$, which exhibit a decreasing frequency mean towards the outlet. For the flows with $j_l = 0.2\ \mathrm{m\,s^{-1}}$, the mean of the slug frequency increases and then decreases with position. Also, even though the mean of the velocity of the liquid in the slug body increases towards the outlet in all these cases, lower values are observed for the cases with the smallest mixture velocity, $j_l + j_g$. In Fig. 11, we present the probability density functions of several variables for the pair $j_l = 0.2\ \mathrm{m\,s^{-1}}$ and $j_g = 2\ \mathrm{m\,s^{-1}}$. The histograms for l_s/d, l_f/d, and ω_s depict the shape of a log-normal distribution.

In Table 4, we report the fraction of merging events discriminated by whether they result from the critical length or critical time criterion or from both criteria simultaneously. The relative number of slug bodies exited at the pipe outlet is also listed. For the same liquid superficial velocity, the relative number of merging events increases with the diminishing of the gas superficial velocity. The majority of merging events are due to the critical length criterion in the cases where $j_l = 2\ \mathrm{m\,s^{-1}}$, whilst merging by the critical time criterion occurs more often in the cases where $j_l = 0.2\ \mathrm{m\,s^{-1}}$. A large relative number of merging events leads to a low relative number of slug bodies exited at the outlet; the opposite also holds. Exiting of the slug bodies at the outlet is always triggered by the critical time criterion — i.e., never by the critical length criterion.

In Fig. 12 we exemplify the local holdup as a function of position at two instants before and two instants after the merging of the 99$^{\mathrm{th}}$ and 100$^{\mathrm{th}}$ cells initiated, for the 600-m long catenary riser and superficial velocities $j_l = j_g = 2\ \mathrm{m\,s^{-1}}$. After merging, the current integer index ordering the cells is reduced by one for the cells upstream of those merged. On the other hand, the integer index given to a slug unit cell at initiation remains unchanged by merging; hence the cell resulting from the coalescence of two others inherit their initiation indexes. In Fig. 12, the cells being merged have initiation indexes of 99 and 100, and the cell arising after merging has thus initiation indexes 99 and 100. The 101$^{\mathrm{th}}$ cell initiated keeps that index, although its current ordering index passes from j to $j-1$. Fig. 13 depicts the dimensionless lengths, l_s/d and l_f/d, for the 100$^{\mathrm{th}}$ cell initiated, before and after merging with the 99$^{\mathrm{th}}$, for $j_l = j_g = 2\ \mathrm{m\,s^{-1}}$, and the 600-m long catenary riser. The coalescence or merging process, governed by the scheme of Section 4.4, is signalled by the sharp, instantaneous change in both lengths. In the case shown, merging is triggered by the critical length and critical time criteria, simultaneously.

5.2. Effect of geometry: Curved versus straight pipes

Here, we investigate the effect on the slug flow dynamics of changing the geometry of the riser. Instead of the curved catenary shape introduced at the beginning of Section 5, we shall consider a straight pipe having the same diameter of that catenary riser. Two cases are considered. First, a straight pipe spanning the chord of the 600 m-long catenary, which is the length of the straight segment joining the end points of the curve. Thus, from the horizontal and vertical projections of the catenary, the length of this pipe is $L = 581.74$ m ($L/d = 2290.3$) and its (constant) inclination angle is 30°. As before, the flow is upwards. Secondly, we consider a horizontal pipe having the length of the horizontal projection of the 600 m-long catenary ($L = 503.80$ m, $L/d = 1983.5$). The temperature, outlet pressure, and fluid properties are the same as those used in the simulations involving the curved riser.

Contour plots of the absolute pressure for the straight inclined and horizontal pipes are presented in Fig. 14 for $j_l = 0.2\ \mathrm{m\,s^{-1}}$ and $j_g = 1\ \mathrm{m\,s^{-1}}$, for the complete length of the pipe and for an interval $0 \leqslant t \leqslant 900$ s. These figures may be compared with Fig. 6(c) for the

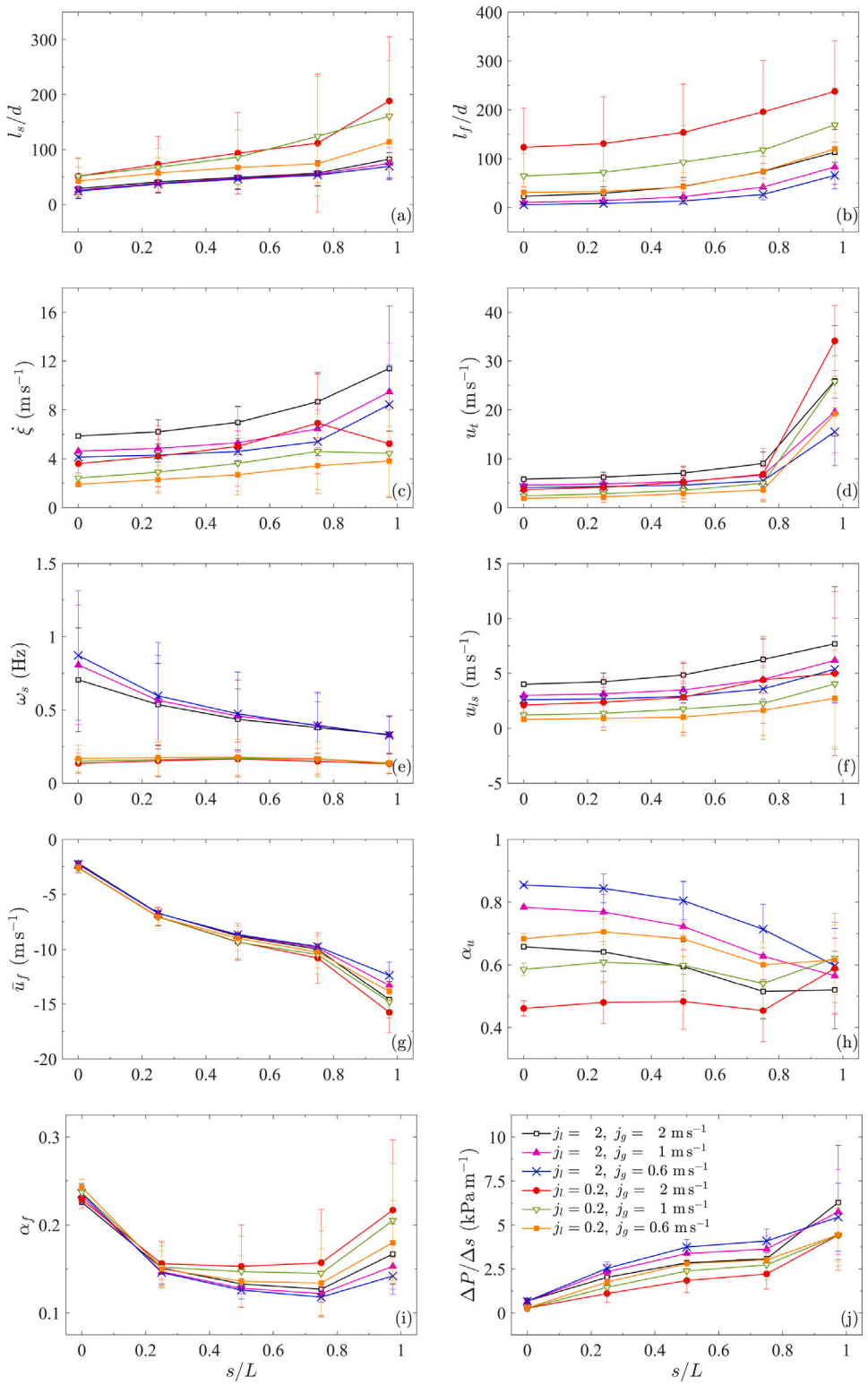

Fig. 9. Slug flow variables at five positions for the 600 m-long catenary riser for various pairs of superficial velocities. The markers represent the mean values and the error bars correspond to the standard deviations.

flow in the curved pipe with the same superficial velocities. Initially, a pressure peak rapidly develops near the inlet in both cases. Then, the pressure decreases leading to an essentially stable behaviour after about 150 s and 200 s for the inclined and horizontal pipes, respectively. The largest pressure values in the catenary and inclined straight pipe are of the same order, whereas in the horizontal pipe, because gravity effects are almost absent, the pressure peak is noticeably smaller. An important observation is that whilst in the case of the catenary, the pressure exhibits conspicuous fluctuations for the period shown, for the straight pipes, the unsteady effects in the pressure are significantly diminished after the initial transient.

Fig. 15 is the counterpart for the straight, inclined and horizontal pipes of Fig. 9. This new figure contains results from two pairs of superficial velocities, $j_l = 2\ \mathrm{m\,s^{-1}}$, $j_g = 2\ \mathrm{m\,s^{-1}}$, and $j_l = 0.2\ \mathrm{m\,s^{-1}}$,

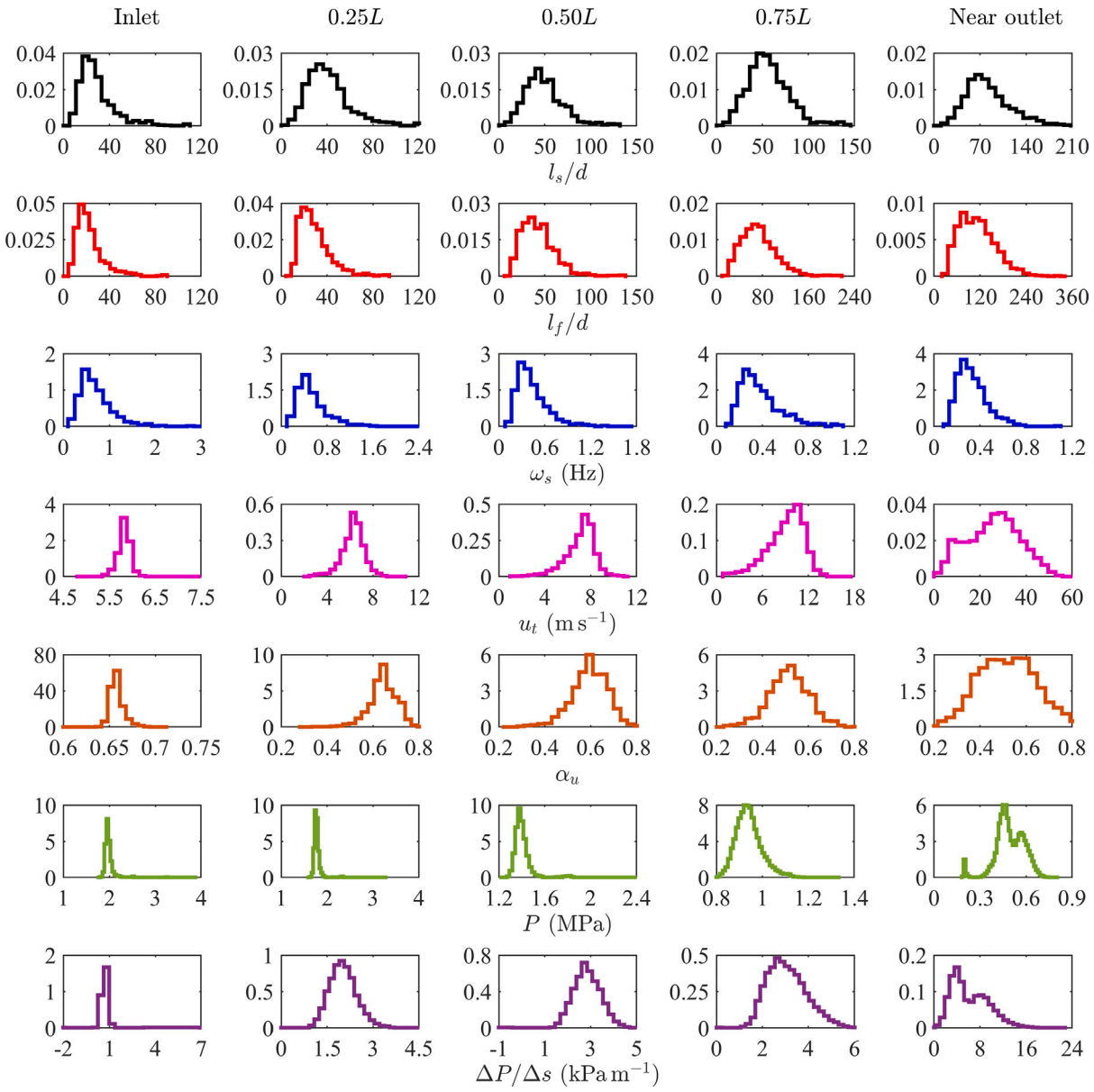

Fig. 10. Probability density functions of several slug flow variables for the 600 m-long catenary riser at five fixed positions measured from the inlet. The location 'near the outlet' corresponds to $0.975L$. The inlet superficial velocities are $j_l = 2$ m s^{-1} and $j_g = 2$ m s^{-1}.

Table 4
Statistics of the slug units merging events and exited slug bodies for the 600 m-long catenary riser.

Superficial velocities (j_l, j_g) (m s^{-1})	Gas–oil ratio (GOR)	Merging events				Exited slug bodies[a] (%)
		Total[a] (%)	Critical length[b] (%)	Critical time[b] (%)	Critical length & time[b] (%)	
(2, 2)	1	47.63	57.81	36.24	5.95	50.33
(2, 1)	0.5	54.48	65.32	30.43	4.24	42.98
(2, 0.6)	0.3	57.36	70.35	24.98	4.68	39.80
(0.2 ,2)	10	4.12	25.00	66.67	8.33	91.41
(0.2, 1)	5	6.25	16.67	83.33	0	75.00
(0.2, 0.6)	3	16.52	27.59	72.41	0	75.50

[a]Normalized with the number of slug units initiated.
[b]Normalized with the total number of merging events.

$j_g = 1$ m s^{-1}, and results from the flow in the 600 m-long catenary are also included for the purpose of discussion. Starting with the case of $j_l = 2$ and $j_g = 2$ m s^{-1}, the variables exhibit features that are similar to those of the catenary. For the inclined straight pipe, however, the magnitude of the means of the average film velocity, the film holdup, and the pressure gradient show little variation in comparison to the catenary. For the catenary, the pressure gradient at the first quarter of the pipe is much smaller than that of the inclined straight pipe.

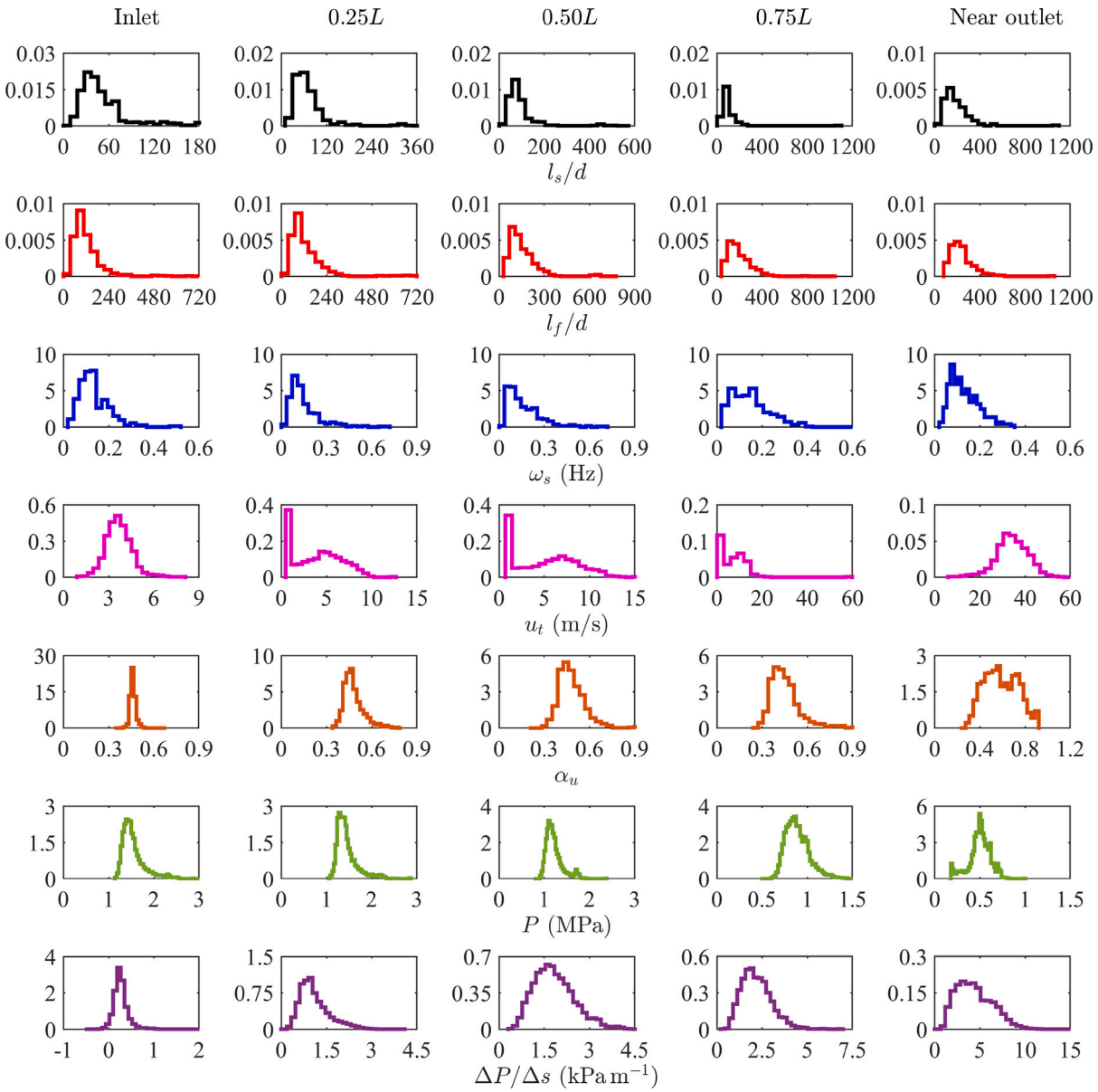

Fig. 11. Probability density functions of several slug flow variables for the 600 m-long catenary riser at five fixed positions measured from the inlet. The location 'near the outlet' corresponds to $0.975L$. The inlet superficial velocities are $j_l = 0.2$ m s^{-1} and $j_g = 2$ m s^{-1}.

This contrasting behaviour is due to the relationship between the pipe inclination and the effect of gravity. The inclination effect also causes a higher mean in the velocity of the backward flow in the film and a thinner holdup in that region for the inclined straight pipe. Note also that the mean of the dimensionless slug body length is smaller for the inclined straight pipe than for the catenary. This contributes to the formation of slug units with a higher frequency for the former. In the case of the horizontal pipe, for the same superficial velocities, most of the variables show similar qualitative trends as the catenary riser and the inclined straight pipe. Unlike the previous cases, for the horizontal pipe, at the inlet, the mean of the film length is higher than that of the slug body length, and this relation remains for the other positions along the pipe. Also, the slug frequency is smaller for the horizontal case than for the catenary and inclined straight pipes. An important quantitative result is that the mean of the average film velocity indicates that the liquid moves forward in this region, in contrast to the catenary and straight inclined pipes, although with a magnitude much smaller than the magnitude in those other cases. In fact, for the horizontal pipe, the mean of the average film velocity is about an order of magnitude smaller than that of the liquid in the slug body, whilst for the catenary and inclined straight pipes, the magnitude of the mean velocity in the film (negative) can be up to twice the mean of the velocity in the slug body. In addition, the pressure gradient is much smaller for the horizontal pipe, as gravitational effects are attenuated in this case in comparison to the catenary and inclined straight cases.

Focusing on the case of superficial velocities $j_l = 0.2$ m s^{-1} and $j_g = 1$ m s^{-1}, for the straight inclined pipe, the overall trends depicted in Fig. 15 of the mean values for $j_l = 0.2$ m s^{-1} and $j_g = 1$ m s^{-1} are similar to those for $j_l = 2$ m s^{-1} and $j_g = 2$ m s^{-1}. For a smaller mixture velocity, the means of the liquid velocity in the slug body, the slug front, and the bubble nose velocities are also lower. Nonetheless, the magnitude of the means of the average film velocity are rather similar. For the case with the lower superficial velocities, the mean of the slug frequency is smaller. For this case, the slug initiation model results in lower means of the slug body and film lengths, but these quantities become larger than those for the highest superficial velocities when the outlet is approached. For the flow with $j_l = 0.2$ m s^{-1} and $j_g = 1$ m s^{-1} in the straight horizontal pipe, the mean values of the dimensionless

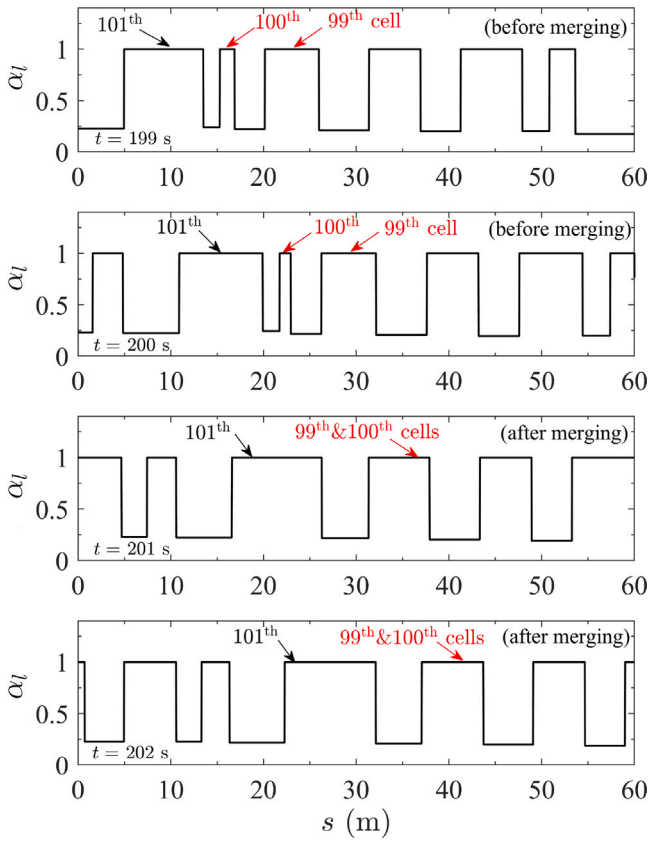

Fig. 12. Local liquid holdup α_l versus position s at four different times for the 600-m long catenary riser and $j_l = j_g = 2$ m s^{-1}. The figures show the merging of the 99th and 100th cells initiated, which occurs at time 200 s $< t <$ 201 s.

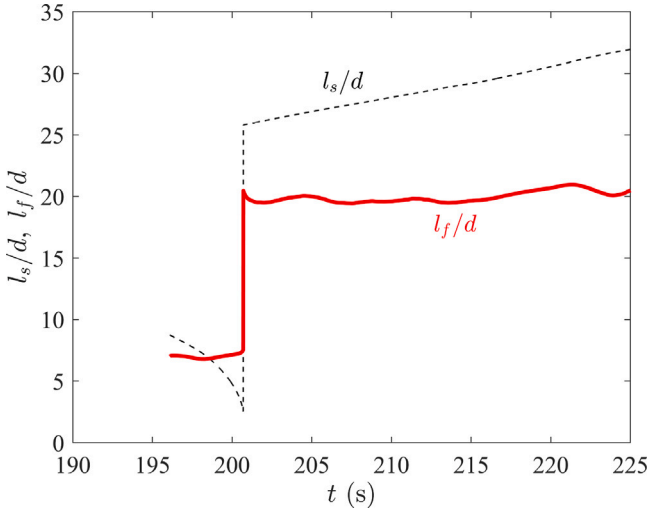

Fig. 13. Dimensionless slug body and film lengths, l_s/d and l_f/d, respectively, as function of time, of the 100th cell initiated for the 600-m long catenary riser and $j_l = j_g = 2$ m s^{-1}.

slug body and, especially, of the film length included in Fig. 15 are much higher than those for $j_l = 2$ m s^{-1} and $j_g = 2$ m s^{-1} in the same configuration. At the inlet, the means of l_s/d and l_f/d are about 3 and 20 times higher for the flow with lower superficial velocities. This corresponds to much longer slug unit cells and hence fewer ones inside the pipe at a given time. Also, the means of the slug frequency and average film velocity are very low, for instance, in comparison to the case with the same superficial velocities in the inclined pipe. When plotting the probability density functions for l_s/d, l_f/d, and the slug frequency, we notice that, at the inlet, these variables do not follow the log-normal distribution (not shown). This is affected by the lower number of unit cells created over the simulated period (see below), which is the same period considered in the simulation of the flow with the same superficial velocities in the inclined straight pipe. Based on flow pattern maps for horizontal gas–liquid flow (e.g., Shoham, 2006), we conclude that the flow is likely to be stratified or stratified-wavy for $j_l = 0.2$ m s^{-1} and $j_g = 1$ m s^{-1}. The results from our model just discussed support this assertion. Since these conditions do not seem to correspond to slug flow, we do not pursue this case further.

Comparing the mean values for the flows with $j_l = 0.2$ m s^{-1} and $j_g = 1$ m s^{-1} in an inclined pipe and in the catenary (discussed in Section 5.1), we observe that most of the variables exhibit similar qualitative behaviours. At the inlet, the mean of l_f/d is greater than that of l_s/d, for the catenary and near the outlet, both attain similar values. For the straight inclined pipe, near the inlet, the relation is reversed, and near the outlet the mean of l_f/d is larger than that of l_s/d. The mean of the frequency for the inclined straight pipe decreases towards the outlet whilst it first increases and then decreases for the catenary riser. The effect of the shape is noticeable for the means of the average film velocity (in magnitude) and the pressure gradient. At the pipe inlet, these values are higher for the pipe with constant inclination than for the catenary; near the outlet, we notice the opposite. This may be explained by the fact that, when compared with the straight inclined pipe, the catenary has a smaller inclination angle at the inlet and a higher one at the outlet.

The physical time simulated for the straight pipes and $j_l = 2$ m s^{-1}, $j_g = 2$ m s^{-1} was $0 \leqslant t \leqslant 2700$ s for both inclinations. In the case of $j_l = 0.2$ m s^{-1}, $j_g = 1$ m s^{-1}, the maximum time was reduced to 900 s.

Some statistics related to the criterion triggering the merging events as well as the relative number of slug bodies exiting the pipe are summarized in Table 5. For the same pair of superficial velocities, a higher relative number of merging events occur for the inclined pipe. For the case with the highest superficial velocities, a slightly greater number of merging events occur due to the critical length criterion than due to the critical time one for both geometrical setups. For the other pair of superficial velocities, the majority of merging events are the result of the critical time criterion. For the top three entries of the table, the slug bodies exited because of the critical time criterion, as in the catenary cases. For the last case, most of the slug bodies exited as a result of the critical length criterion.

5.3. Effect of geometry: Aspect ratio

In this section, we report on the effect of changing the aspect ratio of a catenary riser. To this end, we simulate the gas–liquid slug flow in the catenary geometry employed by Chatjigeorgiou (2017) (see also Ma and Srinil, 2020), which we designate here as the 'longer' catenary, whilst the 600 m-long catenary introduced at the beginning of Section 5 becomes the 'shorter' catenary riser. This longer riser has a length of 2025.70 m, horizontal and vertical projections of 1688 m and 1000 m, and an inclination angle of 1.86° at the inlet section (the same as the shorter catenary). Its chord angle is 30.64° . The corresponding coefficients needed in (49) and (50) are $K_0 = 6.024 \times 10^{-4}$ m^{-1} and $A_0 = 3.247 \times 10^{-2}$. With an inner diameter of 0.385 m, this catenary riser thus has an aspect ratio of $L/d = 5261.6$, which is about twice that of the shorter catenary.

Results from simulations of the slug flow in the longer catenary are presented in Table 6 for several variables. This table also includes the results for the shorter catenary discussed in Section 5.1 for two pairs of superficial velocities, $j_l = 0.2$ m s^{-1} and $j_g = 2$ m s^{-1}, and $j_l = 2$ m s^{-1} and $j_g = 2$ m s^{-1}. The trends exhibited by the values in Table 6 are similar to those observed for the shorter riser. The mean values of the dimensionless slug body and film lengths at the inlet are similar

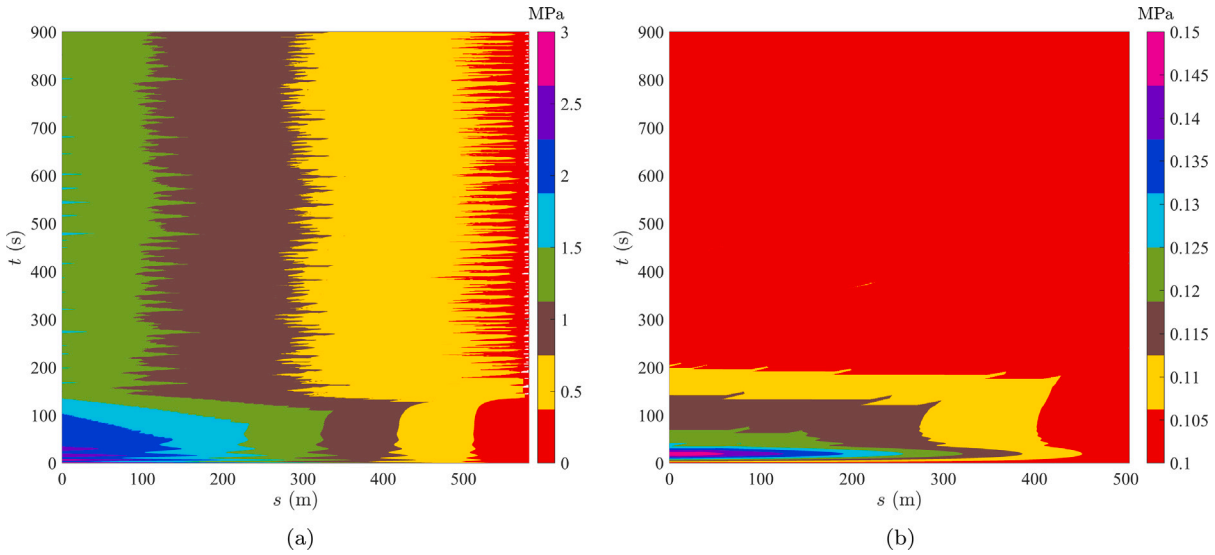

Fig. 14. Contour plots of absolute pressure for the (a) inclined and (b) horizontal straight pipe. The superficial velocities are $j_l = 0.2$ m s^{-1}, $j_g = 1$ m s^{-1} in both cases.

Table 5
Statistics of the slug units merging events and exited slug bodies for the straight pipe geometry.

Superficial velocities	Merging events				Exited slug
(m s^{-1}) (j_l, j_g)	Total[a] (%)	Critical length[b] (%)	Critical time[b] (%)	Critical length & time[b] (%)	bodies[a] (%)
(2, 2) Inclined pipe	58.75	49.56	43.20	7.24	39.57
(2, 2) Horizontal pipe	53.96	47.27	42.90	9.83	44.53
(0.2, 1) Inclined pipe	71.88	7.88	91.30	0.82	20.31
(0.2 ,1) Horizontal pipe	47.37	0	100	0	31.58

[a]Normalized with the number of slug units initiated.
[b]Normalized with the total number of merging events.

between the longer and shorter catenaries, but increase more rapidly for the former, such that by the outlet, the dimensionless lengths for the longer catenary are about twice those for the shorter one. With respect to the means of the various velocities, these values are somewhat higher for the longer catenary. The differences become noticeable towards the outlet, especially for the bubble nose and average film velocities. As for the shorter riser, the average film velocity (negative) indicates a locally backward flow. The mean of the slug frequency is significantly smaller in this longer catenary than in the shorter catenary. By the inlet, it is 30% lower and near the outlet is about 50% smaller. This corresponds to the fact that the change in length for a slug unit is much larger than the change in speeds of both the slug front and the bubble nose. The means of the average unit cell and film holdups, and of the pressure gradient are similar between the two risers. The mean of the absolute pressure is larger for the longer catenary, which has a vertical projection three times greater than that of the shorter one. For the longer catenary, the physical time simulated was again $0 \leqslant t \leqslant 2700$ s. In this case, 1064 slug unit cells were initiated, and 360 cells left the pipe; there were 649 merging events, and 55 unit cells remained in the pipe when the simulation ended.

The statistics regarding the relative number of merging events and slug bodies exited at the outlet for the longer riser are similar to those of the shorter one of Table 4.

6. Conclusions

An improved mechanistic model has been presented for predicting an unsteady gas–liquid upward slug flow in curved inclined rigid pipes using the slug tracking approach. The model, with a sequence of slug unit cells, stems from the mass and momentum conservation laws applied not only to the moving and deforming control volumes enclosing the slug body, the elongated bubble, and the liquid film conforming a unit cell, but also to the surfaces describing the slug bodies fronts and tails. Closure of the model is provided by a correlation for the bubble nose velocity, including the wake effect, which drives coalescence of slug units as a function of the slug body length, and by formulae for the shear stresses at the wall and bubble-film interface.

By assuming that the slug body contains no gas and that the liquid film thickness is spatially uniform, the principle of mass conservation leads to a spatially constant slug liquid velocity and local film and gas velocities varying linearly in space in transient conditions. Mass and momentum balances at the slug body front and bubble nose yield velocity and pressure ‘jumps’.

In the literature on steady or unsteady slug flow modelling, it is not uncommon to modify the pressure drop in a slug unit by adding, in a somewhat heuristic manner, a so-called acceleration pressure drop. This term is given by the difference in momentum fluxes at a certain boundary of the control volume being considered, typically at the slug

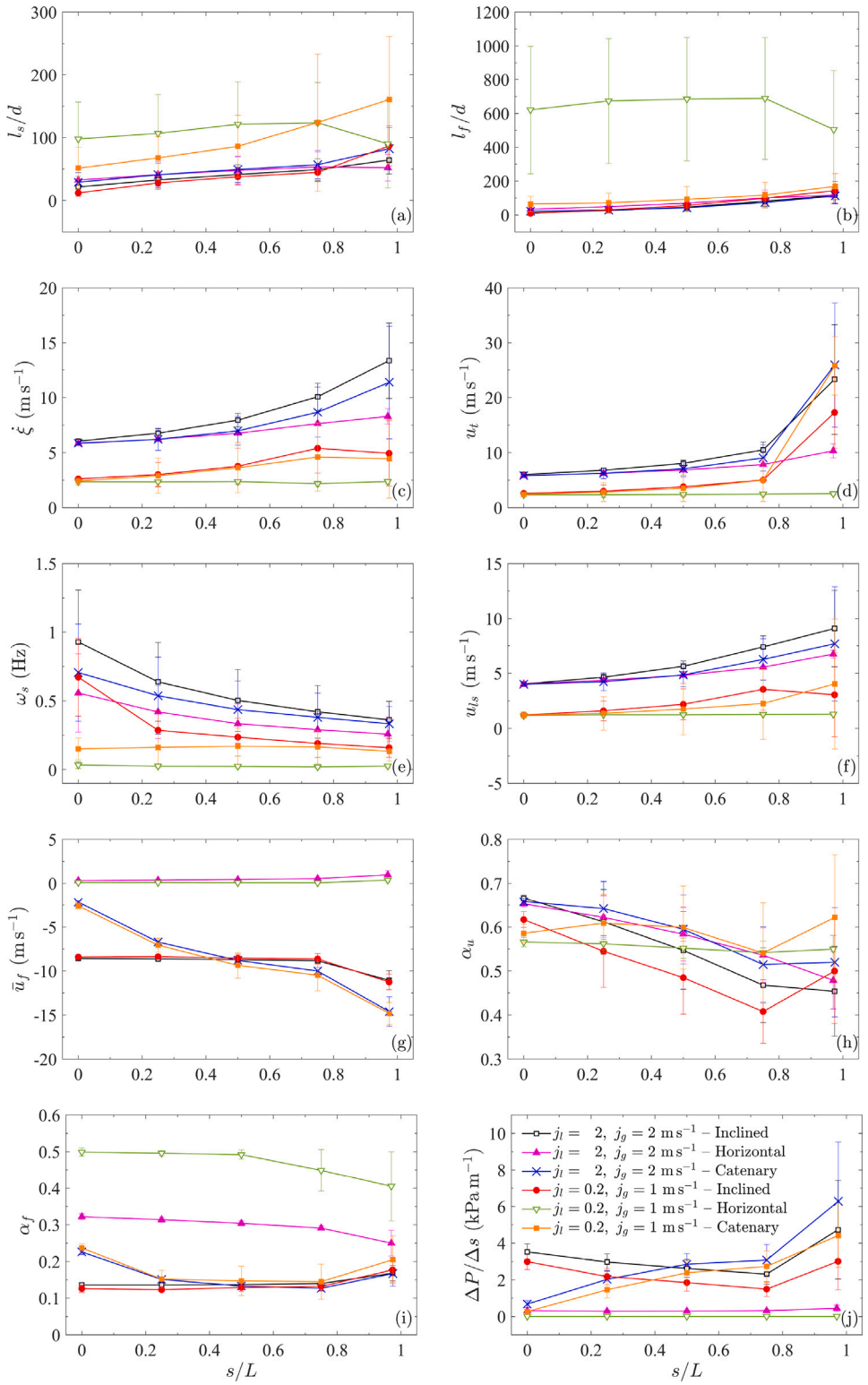

Fig. 15. Slug flow variables at five positions for the inclined and horizontal straight pipes for two pairs of superficial velocities. Results for the 600 m-long catenary are included for comparison. The markers represent the mean values and the error bars correspond to the standard deviations.

front. In the present work, pressure jumps driven by differences in momentum fluxes arise from the formal application of linear momentum balances at the interfaces between the slug body and the elongated bubble-film region. This formalism parallels the application of mass balances at these locations leading to the continuity of mass fluxes for each phase and to velocity jumps. The momentum exchange at the bubble nose is modified, heuristically, to account for a bubble shape that varies gradually rather than sharply. Pressure variation due to hydrostatic effects of the film level is considered.

The slug initiation at the pipe inlet has been considered and is governed by a random process where the slug body length is drawn from a log-normal distribution. The distribution's mean is obtained from a frequency correlation valid for horizontal or inclined pipes. Merging of consecutive slug unit cells is incorporated, taking place

Table 6
Average over time and, in parenthesis, the associated standard deviation of several flow variables for the shorter and longer catenary risers at different positions along their length for $j_l = 2$ m s^{-1} and $j_g = 2$ m s^{-1}. The location 'near the outlet' corresponds to $60\,d$ from the outlet.

Variable	Inlet		$0.25L$		$0.50L$		$0.75L$		Near outlet	
	Shorter pipe	Longer pipe	Shorter pipe	Longer pipe	Shorter pipe	Longer pipe	Shorter pipe	Longer pipe	Shorter pipe	Longer pipe
l_s/d	28.845 (15.523)	28.927 (16.140)	40.949 (18.655)	51.477 (22.195)	49.272 (20.785)	66.988 (25.960)	56.937 (22.525)	77.877 (28.450)	82.277 (33.733)	145.301 (57.773)
l_f/d	22.871 (12.255)	21.724 (11.788)	29.133 (13.499)	34.670 (14.365)	42.992 (18.447)	58.723 (23.390)	73.864 (30.874)	104.361 (40.210)	113.142 (46.877)	223.609 (78.816)
$\dot{\xi}$ (m s^{-1})	5.850 (0.158)	6.055 (0.133)	6.207 (0.990)	6.514 (1.195)	6.977 (1.310)	7.464 (1.617)	8.672 (2.277)	9.722 (2.978)	11.390 (5.125)	11.301 (7.941)
u_t (m s^{-1})	5.815 (0.146)	6.001 (0.124)	6.247 (0.981)	6.407 (1.321)	7.066 (1.301)	7.370 (1.795)	9.030 (2.388)	9.946 (3.356)	25.935 (11.310)	50.638 (14.082)
ω_s (Hz)	0.706 (0.354)	0.496 (0.251)	0.537 (0.280)	0.295 (0.155)	0.436 (0.208)	0.221 (0.116)	0.380 (0.176)	0.191 (0.091)	0.333 (0.127)	0.165 (0.062)
u_{ls} (m s^{-1})	4.007 (0.118)	4.002 (0.091)	4.233 (0.806)	4.315 (0.978)	4.857 (1.074)	5.089 (1.335)	6.264 (1.884)	6.959 (2.497)	7.688 (5.207)	10.476 (10.537)
$\bar{u}_f$ (m s^{-1})	−2.164 (0.120)	−2.635 (0.129)	−6.701 (0.172)	−8.648 (0.176)	−8.786 (0.234)	−11.215 (0.278)	−9.999 (0.405)	−12.849 (0.647)	−14.599 (1.676)	−22.612 (2.026)
α_u	0.658 (0.008)	0.670 (0.008)	0.642 (0.062)	0.649 (0.081)	0.595 (0.079)	0.594 (0.086)	0.515 (0.086)	0.496 (0.091)	0.520 (0.124)	0.537 (0.135)
α_f	0.226 (0.007)	0.232 (0.006)	0.151 (0.007)	0.143 (0.006)	0.133 (0.006)	0.126 (0.005)	0.127 (0.007)	0.121 (0.008)	0.167 (0.034)	0.195 (0.052)
P (MPa)	1.984 (0.105)	5.862 (0.641)	1.780 (0.094)	5.224 (0.620)	1.403 (0.079)	3.984 (0.513)	0.942 (0.057)	2.460 (0.260)	0.496 (0.091))	0.895 (0.264)
$\Delta P/\Delta s$ (kPa m^{-1})	0.677 (0.181)	0.528 (0.149)	2.024 (0.447)	1.926 (0.360)	2.851 (0.582)	2.730 (0.505)	3.078 (0.850)	2.855 (0.726)	6.284 (3.249)	5.854 (3.134)

when the slug body length of the trailing unit cell becomes shorter than a threshold or a time scale criterion has been satisfied. Merging is modelled through balances of mass and momentum. Similar criteria are applied to the slug body withdrawal at the pipe outlet. The system of non-linear equations is numerically solved with a fully implicit approach.

By considering deep-water catenary risers transporting natural gas and oil, when they are initially filled with the flowing single-phase liquid, various combinations of gas and liquid superficial velocities at the inlet have been considered as case studies. Equivalent gas–liquid flows in straight horizontal or inclined pipes have also been studied for the purpose of comparison. Depending on the gas-to-oil superficial velocity ratio (GOR), main findings based on simulation results are summarized as follows.

- Evolution in both space and time of the pressure, local holdup, and liquid and gas velocities has been presented. Upon the introduction of the first slug unit cell, a large pressure peak appeared by the inlet owing to a sudden change in the mixture velocity. This peak is either essentially decayed or paves a way to fluctuations of relatively large amplitudes depending on the superficial velocities. For high GOR, pressure fluctuations, with maximum amplitudes near the inlet, persisted over a long physical time due, presumably, to the gas compressibility effect. Such fluctuating amplitudes seem to significantly increase with GOR.
- For upward flow in curved risers with variable pipe inclinations, the magnitudes of the slug body front, bubble nose, slug body liquid, and film velocities show a strong tendency to increase towards the pipe outlet depending on GOR and the aspect ratio. In the liquid film, the backward flow, due to the pipe inclination, has also been captured.
- When GOR is smaller than one, the mean of the slug frequency decreases towards the outlet.
- For an inclined straight pipe with GOR > 1, after the initial transient dynamics, pressure fluctuations practically vanish in comparison with the same GOR flow in a catenary riser with a chord connecting its ends having the same length and inclination as the straight pipe. For the catenary riser, pressure fluctuations persist over a much longer time interval.
- By simulating catenary risers with two different aspect ratios and subject to the same combination of gas–liquid superficial velocities, the means of the slug body and film lengths, of the bubble nose translational velocity, and of the film velocity (magnitude) are larger for the slug flow in the longer catenary near the outlet. For this longer riser, the mean of the slug frequency is about half of that in the shorter riser at corresponding (relative) positions along the pipe. On the other hand, at these positions, the means of the film holdup and pressure gradients are comparable for the two geometries.

Future work may consider, for curved pipes, a momentum balance for the slug body with an inclination angle different from the one used in the momentum balances for the liquid film and elongated bubble. Also, the presence of gas in the slug bodies, in the form of small bubbles, may be modelled. After implementing aerated slug bodies, the performance of the model with and without the correction in the momentum exchange at the bubble nose may be evaluated. Further, temperature variations may be modelled by including energy balances over the slug body, film, and elongated bubble regions within the framework of the slug tracking approach. Because the model fully accounts for the unsteady fluid mechanics, its coupling with the structural dynamics of a flexible inclined straight or curved riser may advance our understanding of multiphase flow-induced vibration effects and associated flow-structure interaction phenomena.

CRediT authorship contribution statement

Juan C. Padrino: Conceptualization, Methodology, Software, Validation, Formal analysis, Investigation, Data curation, Writing – original draft, Visualization. **Narakorn Srinil:** Conceptualization, Methodology, Resources, Writing – review & editing, Supervision, Project administration, Funding acquisition. **Victoria Kurushina:** Writing – review & editing. **David Swailes:** Writing – review & editing.

Declaration of competing interest

The authors declare that they have no known competing financial interests or personal relationships that could have appeared to influence the work reported in this paper.

Data availability

Data will be made available on request.

Acknowledgements

This research is funded by the Engineering and Physical Sciences Research Council (EPSRC) of the UK Research and Innovation through the "MUltiphase Flow-induced Fluid-flexible structure InteractioN in Subsea applications (MUFFINS)" project grant EP/P033148/1. The authors also thank Yan Aye, a Ph.D. candidate at Newcastle University, for contributing to the wavelet-based frequency plots.

Appendix A. Closure relationships

Following Al-Safran et al. (2004), the bubble nose translational velocity is computed from an expression proposed by Talvy et al. (2000)

$$u_t = u_{t\infty}\left[1 + C_1 \exp(-C_2 l_s/d) + C_3/(l_s/d)\right]; \tag{A.1}$$

the factor in brackets accelerates the bubble nose of a short bubble in the film region. For $u_{t\infty}$, we use the expression by Nicklin (1962)

$$u_{t\infty} = C_s u_{ls} + u_0, \tag{A.2}$$

with the fact that there is no gas in the slug body. Here, $C_s = 1.2$ for turbulent flows and $C_s = 2$ for laminar flows (Fabre, 1994), and for the drift velocity of the elongated bubble, u_0, the expression by Bendiksen (1984) is adopted

$$u_0 = 0.54\sqrt{gd}\cos\theta + 0.35\sqrt{gd}\sin\theta. \tag{A.3}$$

Values for tunning factors C_1, C_2, and C_3 in (A.1) can be found in Al-Safran et al. (2004); they suggest $C_1 = 8$, $C_2 = 1.5$, and $C_3 = 0.5$. Modifications to this model of the translational bubble nose velocity are discussed by Rosa et al. (2015).

Local shear stresses can be determined by

$$\tau_f = f_f \rho_l |u_f| u_f/2, \tag{A.4}$$

$$\tau_g = f_g \rho_g |u_g| u_g/2, \tag{A.5}$$

$$\tau_i = f_i \rho_g |u_g - u_f|\left(u_g - u_f\right)/2, \tag{A.6}$$

$$\tau_s = f_s \rho_l |u_{ls}| u_{ls}/2. \tag{A.7}$$

The (Fanning) friction factors are computed, in the case of smooth pipes, using the Blasius expressions,

$$f_k = C_\tau Re_k^m, \tag{A.8}$$

where $k = f$, g, or s; $C_\tau = 16$ and $m = -1$ for laminar flows, and $C_\tau = 0.046$ and $m = -0.2$ for turbulent flows (Taitel and Dukler, 1976). For rough pipes, we can use expressions for the friction factor that consider the relative roughness. The Reynolds number is computed from

$$Re_f = \frac{\rho_l |u_f| d_f}{\mu_l}, \qquad Re_g = \frac{\rho_g |u_g| d_g}{\mu_g}, \qquad Re_s = \frac{\rho_l |u_{ls}| d}{\mu_l}, \tag{A.9}$$

where

$$d_f = \frac{4A_f}{S_f} \quad \text{and} \quad d_g = \frac{4A_g}{S_g + S_i}. \tag{A.10}$$

The friction factor f_i is also computed with (A.8) based on a Reynolds number $Re_i = \rho_g |u_g - u_f| d_g/\mu_g$. Once the local shear stresses have been determined, the average shear stresses $\overline{\tau}_f$, $\overline{\tau}_g$, and $\overline{\tau}_i$ can be computed by integration over the length of the elongated bubble-film region.

An additional closure relationship, in this case for the slug frequency, is given in Section 3.1. This is employed to obtain the slug body length when a unit cell is initiated.

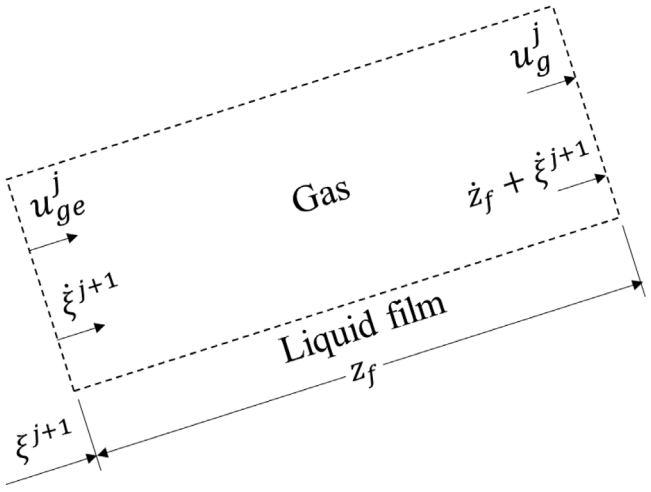

Fig. B.1. Moving control volume enclosed in the elongated bubble of unit cell j with its left boundary fixed to the bubble rear and its right boundary at an arbitrary distance z_f from the left edge.

Appendix B. Gas and liquid velocities in elongated bubble and film regions

Consider the control volume enclosed in the elongated bubble depicted in Fig. B.1. The left surface is at position ξ^{j+1} and moves with the bubble rear at the speed $\dot{\xi}^{j+1}$; the right surface is within the bubble at an arbitrary position $z_f + \xi^{j+1}$ and moves with the velocity $\dot{z}_f + \dot{\xi}^{j+1}$. This control volume is also bounded by the pipe inner wall and the gas–liquid interface. If $u_g(z_f)$ is the gas axial velocity at $z_f + \xi^{j+1}$, the mass balance for the gas in this control volume can be written as

$$\frac{d}{dt}\left(\rho_g^j \alpha_g^j z_f A\right) = \rho_g^j \alpha_g^j A\left(u_{ge}^j - \dot{\xi}^{j+1}\right) - \rho_g^j \alpha_g^j A\left(u_g^j - \dot{z}_f - \dot{\xi}^{j+1}\right). \tag{B.1}$$

In writing Eq. (B.1), we have assumed that the gas volume fraction is the same at every cross section in the control volume (consistent with the uniform film thickness assumption). With this hypothesis, the effects on the volume fraction of the variation of the interface profile, especially near the bubble nose, are neglected. Expanding the left-hand side of (B.1) and rearranging, this expression becomes

$$z_f \frac{d}{dt}\left(\rho_g^j \alpha_g^j\right) = \rho_g^j \alpha_g^j \left(u_{ge}^j - u_g^j\right), \tag{B.2}$$

and the terms with $\dot{z}_f$ cancel out. By invoking Eq. (7) for the mass balance of gas over the entire elongated bubble, we can eliminate the time derivative in Eq. (B.2) and arrive at Eq. (9) for the gas velocity. A similar procedure for the liquid film leads to Eq. (10) for the liquid velocity in this region.

Appendix C. Geometric expressions

With the aid of Fig. 2, we may write several geometric relations among the variables appearing in the model for a given slug unit cell. For a differential element of cross-sectional area, we may write $dA = d\sqrt{1 - (2\zeta/d - 1)^2}\, d\zeta$. Then, the liquid volume fraction can be expressed in terms of the dimensionless film thickness h_f/d as

$$\alpha_f = \frac{1}{A}\int_{A_f} dA = \frac{2}{\pi}\left[\left(\frac{2h_f}{d} - 1\right)\sqrt{\frac{h_f}{d} - \left(\frac{h_f}{d}\right)^2} + \sin^{-1}\sqrt{\frac{h_f}{d}}\right]. \tag{C.1}$$

Furthermore, the integrals in Eq. (25) can be evaluated, leading to

$$\Sigma_f = \frac{d}{\pi\alpha_f}\left[\frac{\left(2 + (2h_f/d - 1)^2\right)}{3}\sqrt{\frac{h_f}{d} - \left(\frac{h_f}{d}\right)^2} + \left(\frac{2h_f}{d} - 1\right)\sin^{-1}\sqrt{\frac{h_f}{d}}\right], \tag{C.2}$$

$$\Sigma_g = \frac{d}{\pi\alpha_g}\left[\frac{(2+(2h_f/d-1)^2)}{3}\sqrt{\frac{h_f}{d}-\left(\frac{h_f}{d}\right)^2}-\left(\frac{2h_f}{d}-1\right)\cos^{-1}\sqrt{\frac{h_f}{d}}\right]. \tag{C.3}$$

The length of the gas–liquid interface in the cross section can be determined from

$$S_i = d\sqrt{1-(1-2h_f/d)^2}. \tag{C.4}$$

The wetted perimeters of the liquid film and the elongated bubble, S_f and S_g, respectively, are given by

$$S_f = \lambda\, d/2, \qquad S_g = \pi d - S_f, \tag{C.5}$$

where λ, the angle of the circular sector subtended by the interface (see Fig. 2), is related to the film thickness by $\sin(\lambda/2) = 1 - 2h_f/d$.

Since an inclination angle θ^j is the angle subtended by the straight segment connecting points ξ^j and ξ^{j+1}, which fall on the axis of the curved pipe, and the horizontal x-axis, one can write

$$\theta^j = \tan^{-1}\left[\frac{y(\xi^j)-y(\xi^{j+1})}{x(\xi^j)-x(\xi^{j+1})}\right]. \tag{C.6}$$

References

Al-Safran, E., 2009. Prediction of slug liquid holdup in horizontal pipes. J. Energy Resour. Technol. 131 (2), 023001.

Al-Safran, E.M., Sarica, C., Zhang, H.-Q., Brill, J.P., 2005. Probabilistic/mechanistic modeling of slug length distribution in a horizontal pipeline. SPE Prod. Facil. 20 (02), 160–172.

Al-Safran, E., Taitel, Y., Brill, J., 2004. Prediction of slug length distribution along a hilly terrain pipeline using slug tracking model. J. Energy Resour. Technol. 126 (1), 54–62.

Andreussi, P., Bendiksen, K., 1989. An investigation of void fraction in liquid slugs for horizontal and inclined gas—liquid pipe flow. Int. J. Multiph. Flow 15 (6), 937–946.

Barnea, D., 1990. Effect of bubble shape on pressure drop calculations in vertical slug flow. Int. J. Multiph. Flow. 16 (1), 79–89.

Barnea, D., Brauner, N., 1985. Holdup of the liquid slug in two phase intermittent flow. Int. J. Multiph. Flow. 11 (1), 43–49.

Barnea, D., Shoham, O., Taitel, Y., Dukler, A., 1980. Flow pattern transition for gas-liquid flow in horizontal and inclined pipes. Comparison of experimental data with theory. Int. J. Multiph. Flow 6 (3), 217–225.

Barnea, D., Taitel, Y., 1993. A model for slug length distribution in gas-liquid slug flow. Int. J. Multiph. Flow. 19 (5), 829–838.

Batchvarov, A., Kahouadji, L., Magnini, M., Constante-Amores, C., Shin, S., Chergui, J., Juric, D., Craster, R., Matar, O., 2020. Effect of surfactant on elongated bubbles in capillary tubes at high Reynolds number. Phys. Rev. Fluids 5 (9), 093605.

Bendiksen, K.H., 1984. An experimental investigation of the motion of long bubbles in inclined tubes. Int. J. Multiph. Flow. 10 (4), 467–483.

Bendiksen, K., Maines, D., Moe, R., Nuland, S., 1991. The dynamic two-fluid model OLGA: Theory and application. SPE Prod. Eng. 6 (02), 171–180, SPE-19451-PA.

Bonizzi, M., Andreussi, P., Banerjee, S., 2009. Flow regime independent, high resolution multi-field modelling of near-horizontal gas–liquid flows in pipelines. Int. J. Multiph. Flow. 35 (1), 34–46.

Brill, J., Schmidt, Z., Coberly, W., Herring, J., Moore, D., 1981. Analysis of two-phase tests in large-diameter flow lines in Prudhoe Bay field. Soc. Petroleum Eng. J. 21 (03), 363–378.

Brustur, A.-G., 2014. Multiphase flow in pipelines: An analysis of the influence of empirical correlations on mechanistic models (Ph.D. thesis). Curtin University.

Chatjigeorgiou, I.K., 2017. Hydroelastic response of marine risers subjected to internal slug-flow. Appl. Ocean Res. 62, 1–17.

Constante-Amores, C., Kahouadji, L., Batchvarov, A., Shin, S., Chergui, J., Juric, D., Matar, O., 2021. Dynamics of a surfactant-laden bubble bursting through an interface. J. Fluid Mech. 911, A57.

Danielson, T., Bansal, K.M., Hansen, R., Leporcher, E., 2005. LEDA: The next multiphase flow performance simulator. In: 12th International Conference on Multiphase Production Technology. OnePetro.

Dukler, A., Hubbard, M., 1975. A model for gas-liquid slug flow in horizontal and near horizontal tubes. Ind. Eng. Chem. Fundam. 14 (4), 337–347.

Fabre, J., 1994. Advancements in two-phase slug flow modeling. In: University of Tulsa Centennial Petroleum Engineering Symposium. Society of Petroleum Engineers.

Fabre, J., Liné, A., 1992. Modeling of two-phase slug flow. Annu. Rev. Fluid Mech. 24 (1), 21–46.

Fan, Y., Pereyra, E., Sarica, C., Schleicher, E., Hampel, U., 2019. Analysis of flow pattern transition from segregated to slug flow in upward inclined pipes. Int. J. Multiph. Flow. 115, 19–39.

Felizola, H., 1992. Slug flow in extended reach directional wells (Masters thesis). University of Tulsa.

Ferrari, M., Bonzanini, A., Poesio, P., 2019. A slug capturing method in unconventional scenarios: The 5ESCARGOTS code applied to non-Newtonian fluids, high viscous oils and complex geometries. Petroleum 5 (2), 171–177.

Ferziger, J., Perić, M., 2002. Computational Methods for Fluid Dynamics, third ed. Springer.

Gomez, L., Shoham, O., Schmidt, Z., Chokshi, R., Northug, T., 2000. Unified mechanistic model for steady-state two-phase flow: Horizontal to vertical upward flow. SPE J. 5 (03), 339–350.

Gordon, I., Fairhurst, C.P., 1987. Multi-phase pipeline and equipment design for marginal and deep water field development. In: Proceedings of the 3rd International Conference on Multi-Phase Flow, Paper Al, the Hague, Netherlands, May 18–20.

Gregory, G., Nicholson, M., Aziz, K., 1978. Correlation of the liquid volume fraction in the slug for horizontal gas-liquid slug flow. Int. J. Multiph. Flow. 4 (1), 33–39.

Grigoleto, M.M., Bassani, C.L., Conte, M.G., Cozin, C., Barbuto, F.A., Morales, R.E., 2021. Heat transfer modeling of non-boiling gas-liquid slug flow using a slug tracking approach. Int. J. Heat Mass Transfer 165, 120664.

Grolman, E., Fortuin, J., 1997. Gas-liquid flow in slightly inclined pipes. Chem. Eng. Sci. 52 (24), 4461–4471.

Heaney, C., Wolffs, Z., Tómasson, J., Kahouadji, L., Salinas, P., Nicolle, A., Navon, I., Matar, O., Srinil, N., Pain, C., 2022. An AI-based non-intrusive reduced-order model for extended domains applied to multiphase flow in pipes. Phys. Fluids 34 (5), 055111.

Hernandez-Perez, V., 2007. Gas-Liquid Two-Phase Flow in Inclined Pipes (Ph.D. thesis). University of Nottingham, Nottingham, United Kingdom, See also URL http://eprints.nottingham.ac.uk/11764/. (Visited 28 April 2021).

Hirt, C., Nichols, B., 1981. Volume of fluid (VOF) method for the dynamics of free boundaries. J. Comput. Phys. 39 (1), 201–225.

Irfansyah, T., Widyoko, B., Gunarwan, G., Lopez, D., 2005. Simulation of multiphase flows in Indonesian pipelines: Comparison of TACITE and OLGA results. In: 12th International Conference on Multiphase Production Technology. May 25–27, BHR-2005-H3.

Issa, R., Kempf, M., 2003. Simulation of slug flow in horizontal and nearly horizontal pipes with the two-fluid model. Int. J. Multiph. Flow. 29 (1), 69–95.

Katsikadelis, J.T., 2016. The Boundary Element Method for Engineers and Scientists: Theory and Applications. Academic Press.

Kjeldby, T., Henkes, R., Nydal, O., 2011. Slug tracking simulation of severe slugging experiments. World Acad. Sci. Eng. Technol. 78, 928–933.

Kjeldby, T., Nydal, O., 2012. Modeling of two phase flow expansion instabilities in long risers or wells. In: HEFAT 2012.

Kjølaas, J., 2007. Plug propagation in multiphase pipelines: Modeling and small scale experiments (Ph.D. thesis). Norwegian University of Science and Technology.

Klinkenberg, A.M., Tijsseling, A.S., 2021. Stochastic mechanistic modelling of two-phase slug flow forces on bends in horizontal piping. Int. J. Multiph. Flow. 144, 103778.

Kordyban, E., 1961. A flow model for two-phase slug flow in horizontal tubes. J. Basic Eng. 83 (4), 613–618.

Krasnopolsky, B.I., Lukyanov, A.A., 2018. A conservative fully implicit algorithm for predicting slug flows. J. Comput. Phys. 355, 597–619.

Larsen, M., Hustvedt, E., Hedne, P., Straume, T., 1997. PeTra: A novel computer code for simulation of slug flow. In: SPE Annual Technical Conference and Exhibition. October 5–8, SPE-38841-MS.

Ma, B., Srinil, N., 2020. Planar dynamics of inclined curved flexible riser carrying slug liquid–gas flows. J. Fluids Struct. 94, 102911.

Mandhane, J., Gregory, G., Aziz, K., 1974. A flow pattern map for gas—liquid flow in horizontal pipes. Int. J. Multiph. Flow 1 (4), 537–553.

Mazza, R., Rosa, E., Yoshizawa, C., 2010. Analyses of liquid film models applied to horizontal and near horizontal gas–liquid slug flows. Chem. Eng. Sci. 65 (12), 3876–3892.

Meng, W., 1999. Low Liquid Loading Gas-Liquid Two-Phase Flow in Near-Horizontal Pipes. The University of Tulsa.

Mohammadi, S., Papa, M., Pereyra, E., Sarica, C., 2019. Genetic algorithm to select a set of closure relationships in multiphase flow models. J. Pet. Sci. Eng. 181, 106224.

Moin, P., 2010. Fundamentals of Engineering Numerical Analysis. Cambridge University Press.

Mukherjee, H., Brill, J., 1985. Pressure drop correlations for inclined two-phase flow. J. Energy Resour. Technol. 107, 549–554.

Nicklin, D., 1962. Two-phase bubble flow. Chem. Eng. Sci. 17 (9), 693–702.

Nydal, O., 2012. Dynamic models in multiphase flow. Energy Fuels 26 (7), 4117–4123.

Nydal, O., Banerjee, S., 1996. Dynamic slug tracking simulations for gas-liquid flow in pipelines. Chem. Eng. Commun. 141 (1), 13–39.

Ortega, A., Rivera, A., Larsen, C., 2013. Flexible riser response induced by combined slug flow and wave loads. In: International Conference on Offshore Mechanics and Arctic Engineering. American Society of Mechanical Engineers, June 9–14, OMAE2013-10891, V04BT04A008.

Ortega, A., Rivera, A., Larsen, C., 2018. Slug flow and waves induced motions in flexible riser. J. Offshore Mech. Arct. Eng. 140 (1).

Ortega, A., Rivera, A., Nydal, O., Larsen, C., 2012. On the dynamic response of flexible risers caused by internal slug flow. In: International Conference on Offshore Mechanics and Arctic Engineering. American Society of Mechanical Engineers, pp. 647–656, July 1–6, OMAE2012-83316.

Padrino, J.C., Srinil, N., Kurushina, V., Swailes, D., Pain, C.C., Matar, O.K., 2021. A one-dimensional mechanistic model for tracking unsteady slug flow. In: Proceedings of the ASME 2021 International Mechanical Engineering Congress and Exposition IMECE2021. American Society of Mechanical Engineers, Virtual, Online, November 1–5.

Panton, R., 2013. Incompressible flow, fourth ed. John Wiley & Sons.

Petalas, N., Aziz, K., 2000. A mechanistic model for multiphase flow in pipes. J. Can. Petrol. Technol. 39 (06), 43–55.

Prosperetti, A., Tryggvason, G. (Eds.), 2009. Computational Methods for Multiphase Flow. Cambridge University Press.

Renault, F., 2007. A Lagrangian slug capturing scheme for gas-liquid flows in pipes (Ph.D. thesis). Norwegian University of Science and Technology.

Rosa, E., Mazza, R., Morales, R., Rodrigues, H., Cozin, C., 2015. Analysis of slug tracking model for gas–liquid flows in a pipe. J. Braz. Soc. Mech. Sci. Eng. 37 (6), 1665–1686.

Roullier, D., Shippen, M., Adames, P., Pereyra, E., Sarica, C., 2017. Identification of optimum closure relationships for a mechanistic model using a data set from a low-liquid loading subsea pipeline. In: SPE Annual Technical Conference and Exhibition. October 9–11, SPE-187327-MS.

Schulkes, R., 2011. Slug frequencies revisited. In: 15th International Conference on Multiphase Production Technology. BHR Group.

Shin, S., Chergui, J., Juric, D., Kahouadji, L., Matar, O., Craster, R., 2018. A hybrid interface tracking–level set technique for multiphase flow with soluble surfactant. J. Comput. Phys. 359, 409–435.

Shoham, O., 2006. Mechanistic modeling of gas-liquid two-phase flow in pipes. Society of Petroleum Engineers, Richardson, TX.

Sivier, S., Loth, E., Baum, J., Löhner, R., 1993. Eulerian-Eulerian and Eulerian-Lagrangian methods in two phase flow. In: Thirteenth International Conference on Numerical Methods in Fluid Dynamics. Springer, pp. 473–477.

Spedding, P., 1980. Regime maps for air water two phase flow. Chem. Eng. Sci. 35 (4), 779–793.

Street, R.L., Watters, G.Z., Vennard, J.K., 1996. Elementary Fluid Mechanics, seventh ed. John Wiley & Sons.

Taitel, Y., Barnea, D., 1990a. A consistent approach for calculating pressure drop in inclined slug flow. Chem. Eng. Sci. 45 (5), 1199–1206.

Taitel, Y., Barnea, D., 1990b. Two-phase slug flow. Adv. Heat Trans. 20 (1), 83–132.

Taitel, Y., Barnea, D., 1998. Effect of gas compressibility on a slug tracking model. Chem. Eng. Sci. 53 (11), 2089–2097.

Taitel, Y., Dukler, A., 1976. A model for predicting flow regime transitions in horizontal and near horizontal gas-liquid flow. AIChE J. 22 (1), 47–55.

Talvy, C., Shemer, L., Barnea, D., 2000. On the interaction between two consecutive elongated bubbles in a vertical pipe. Int. J. Multiph. Flow. 26 (12), 1905–1923.

Théron, B., 1989. Ecoulements diphasiques instationnaires en conduite horizontale (Ph.D. thesis). Toulouse, INPT.

Ujang, P., Lawrence, C., Hewitt, G., 2006. Conservative incompressible slug tracking model for gas-liquid flow in a pipe. BHR Group Multiph. Technol. 5, 375–388.

Valdés, J., Kahouadji, L., Matar, O., 2022. Current advances in liquid–liquid mixing in static mixers: A review. Chem. Eng. Res. Des. 177, 694–731.

Vásquez, J.A.M., Avila, J.P.J., 2021. Three-dimensional dynamic behaviour of flexible catenary risers with an internal slug flow. J. Fluids Struct. 107, 103409.

Wu, B., Firouzi, M., Mitchell, T., Rufford, T., Leonardi, C., Towler, B., 2017. A critical review of flow maps for gas-liquid flows in vertical pipes and annuli. Chem. Eng. J. 326, 350–377.

Xin, W., Liejin, G., Zhang, X., 2006. Development of liquid slug length in gas-liquid slug flow along horizontal pipeline: experiment and simulation. Chin. J. Chem. Eng. 14 (5), 626–633.

Zanganeh, H., Kurushina, V., Srinil, N., Matar, O., 2020. Influence of combined empirical functions on slug flow predictions of pipelines with variable inclinations. In: International Conference on Offshore Mechanics and Arctic Engineering. vol. 84355, American Society of Mechanical Engineers, V004T04A025.

Zhang, H.-Q., Jayawardena, S., Redus, C., Brill, J., 2000. Slug dynamics in gas-liquid pipe flow. J. Energy Resour. Technol. 122 (1), 14–21.

Zhang, H.-Q., Wang, Q., Sarica, C., Brill, J., 2003a. Unified model for gas-liquid pipe flow via slug dynamics – Part 1: Model development. J. Energy Resour. Technol. 125 (4), 266–273.

Zhang, H.-Q., Wang, Q., Sarica, C., Brill, J., 2003b. Unified model for gas-liquid pipe flow via slug dynamics – Part 2: Model validation. J. Energy Resour. Technol. 125, 274–283.

Zheng, G., Brill, J., Taitel, Y., 1994. Slug flow behavior in a hilly terrain pipeline. Int. J. Multiph. Flow 20 (1), 63–79.

Zikanov, O., 2019. Essential Computational Fluid Dynamics. John Wiley & Sons.